Hydrate Evolution in Response to Ongoing Environmental Shifts

CONTRACT NO. DE-FE0013565

FINAL PROJECT REPORT
Reporting Period: January 1, 2014 to December 31, 2015

Prepared by
Alan W. Rempel
Department of Geological Sciences
University of Oregon
1272 University of Oregon
Eugene, OR 97405
Phone: 541-346-6316
Email: rempel@uoregon.edu

Recipient Organization
Sponsored Project Services
5219 University of Oregon
Eugene, OR 97403-5219
DUNS Number: 948117312

Prepared for
U. S. Department of Energy
National Energy Technology Laboratory
3610 Collins Ferry Road
P.O. Box 880 Morgantown, WV 26508

Project Manager
Adam Tew
Adam.Tew@netl.doe.gov

Acknowledgment: "This material is based upon work supported by the Department of Energy under Award Number DE-FE0013565."

Abstract

Natural gas hydrates have the potential to become a vital domestic clean-burning energy source. However, past changes in environmental conditions have caused hydrates to become unstable and trigger both massive submarine landslides and the development of crater-like pockmarks, thereby releasing methane into the overlying seawater and atmosphere, where it acts as a powerful greenhouse gas. This project was designed to fill critical gaps in our understanding of domestic hydrate resources and improve forecasts for their response to environmental shifts. Project work can be separated into three interrelated components, each involving the development of predictive mathematical models. The first project component concerns the role of sediment properties on the development and dissociation of concentrated hydrate anomalies. To this end, we developed numerical models to predict equilibrium solubility of methane in two-phase equilibrium with hydrate as a function of measureable porous medium characteristics. The second project component concerned the evolution of hydrate distribution in heterogeneous reservoirs. To this end, we developed numerical models to predict the growth and decay of anomalies in representative physical environments. The third project component concerned the stability of hydrate-bearing slopes under changing environmental conditions. To this end, we developed numerical treatments of pore pressure evolution and consolidation, then used "infinite-slope" analysis to approximate the landslide potential in representative physical environments, and developed a "rate-and-state" frictional formulation to assess the stability of finite slip patches that are hypothesized to develop in response to the dissociation of hydrate anomalies. The increased predictive capabilities that result from this work provide a framework for interpreting field observations of hydrate anomalies in terms of the history of environmental forcing that led to their development. Moreover, by taking explicit account of anomaly dissociation, project results are designed to help improve forecasts for changes in slope stability that could pose significant threats to energy infrastructure, disrupt hydrate reserves, and pollute the atmosphere with vast quantities of methane. This report presents the details of our work and outlines some of the highlights from our findings.

TABLE OF CONTENTS

Executive Summary

The objective of this project is to quantitatively assess how climate change alters both reservoir hydrate distribution and gas transport into the overlying ocean and atmosphere. Over the two-year duration of funding, the HEROES team devoted our efforts to several distinct, inter-related topics that contribute towards this central goal. This final report concentrates on three specific problems that constitute the primary publishable results generated by the three project graduate students in collaboration with the PI.

Section I describes our model for the effects of porous media characteristics on two-phase hydrate equilibrium conditions. We show how the geometrical limitations on hydrate growth imposed by the porous matrix can be predicted quantitatively in terms of perturbations to the equilibrium methane solubility in the residual pore waters. Validation tests confirm excellent agreement between model predictions and laboratory data on analog systems, providing confidence in our ability to translate our understanding of the controlling microphysical interactions into macroscopically relevant treatments of phase behavior within natural hydrate reservoirs.

In **Section II**, we combine a simplified treatment of the solubility effects described in **Section I** together with an analysis of porous flow near a dipping coarse-grained layer to describe the detailed distribution of hydrate accumulation through time. This idealized model provides a quantitative understanding for the factors that control hydrate reservoir characteristics. At present, qualitative comparisons with the published characteristics of hydrate anomalies reported in diverse locations lend credence to the model results. Detailed high-resolution hydrate saturation data and depositional histories should enable more compelling quantitative validation tests in the future.

In **Section III**, we consider the implications of hydrate dissociation on slope stability. A paper describing the details of our new formulation for how "rate-weakening friction characterizes both slow sliding and catastrophic failure of landslides" is in revision for *Proceedings of the National Academy of Sciences"*. Here, we build upon that work to consider how the loss of cohesion and changes in pore pressure that accompany dissociation of hydrate anomalies similar to those modeled in **Section II** can lead to different outcomes, ranging from static conditions to slow sliding to catastrophic failure.

In **Section IV**, we offer concluding remarks that include a brief outline of some of our other efforts that have not yet reached the publishable stage. Though funding to continue research in these areas has expired, we continue to make progress and hope to redouble our efforts as time and resources allow in the near to intermediate future.

I. The effects of pore geometry on gas hydrate stability

This section concerns modifications to the two-phase hydrate-liquid equilibrium conditions that result from confinement in fine-grained pores and the exclusion of dissolved salts from the crystal lattice. This portion of our study constituted a majority of the 2015 MSc. thesis of University of Oregon graduate student, Julia Irizarry; a condensed and modified version will be submitted for publication in a peer-reviewed journal as "Modeling the effects of pore geometry and salinity on the solidification of gas hydrates and water ice", by Julia T. Irizarry and Alan W. Rempel.

I.1. Introduction

Gas hydrates are ice-like compounds that form on continental shelves from mixtures of methane and water. The sedimentary porous media that host gas hydrates modify the two-phase equilibrium conditions of the hydrate-liquid system (Clennell et al., 1999; Cook and Malinverno, 2013; Daigle and Dugan, 2011; Rempel, 2011). The phase equilibrium shifts from bulk phase equilibrium for two primary reasons: first, because the complex pore geometry forces the hydrate-liquid interface to curve (**Fig. I.1**) and so increases the surface energy in proportion to the enhanced surface area, and second, because of the intermolecular forces that induce liquid water to wet the interfaces between sediment particles and hydrate crystals (Rempel, 2011). Similar behavior is important in vapor-water systems, where the pore volume fraction occupied by liquid (i.e. the liquid saturation) depends on the matric potential, which is defined as the pressure difference between the non-wetting vapor phase and the wetting liquid phase (e.g. Or and Tuller, 1999). In ice-water systems the effects of curvature and wetting facilitate the stable equilibrium presence of residual liquid with a saturation that depends on the undercooling ΔT, which is defined as the temperature depression below the normal melting point (e.g. Rempel, 2012). Our focus is on hydrate behavior, but these other systems deserve mention here because we use them below in tests to validate our numerical procedure. Below, we describe our approach, model validation tests, and how our model can be applied to hydrate-liquid systems.

We developed a computational method for predicting the shift in phase equilibrium in three-dimensional porous media. Our codes are designed to: a) synthetically produce a packing of poly-dispersed spherical particles with a specified distribution of sizes, b) determine the geometrical constraints on hydrate phase-equilibrium at any given point within the pore space, and c) quantify the effects of these constraints in modifying the phase behavior for a specified model. The presence of dissolved impurities that are excluded from the crystalline hydrate lattice is an added complication that is both important in sub-seafloor sediments and easily handled by our model; we have explored these effects, but will not discuss them in detail here.

Several models have been developed that simplify the pore geometry while still capturing some effects of the porous medium on phase behavior. Pore geometry is most commonly modeled by approximating pores as circular cylinders (Denoyel and Pellenq, 2002; Millington and Quirk, 1961; Mualem, 1976; Wilder et al., 2001). Other approaches include the use of circular or spherical pores connected by narrow cylindrical pore throats (Liu and Flemings, 2011), triangular pores (Rempel, 2011), and random packings of circles (Rempel, 2012). To add a further degree of realism, we develop a sphere-packing tool in MATLAB that creates a three-dimensional porous medium to emulate arrangements of sedimentary particles. We use the three-dimensional pore geometry created by our algorithm to predict the perturbations to the phase behavior that result. Even for idealized simple cubic and face-centered cubic packing, fully evaluating the shape of the evolving three-dimensional interphase geometry can become remarkably complex (Cahn et al., 1992). However, we have developed a simpler approach that avoids calculating the evolving geometry of the entire phase boundary, but instead samples a sequence of discrete points within the synthetic pore space and approximates the local geometry of the interface under the conditions when hydrate first becomes stable at each sampled location.

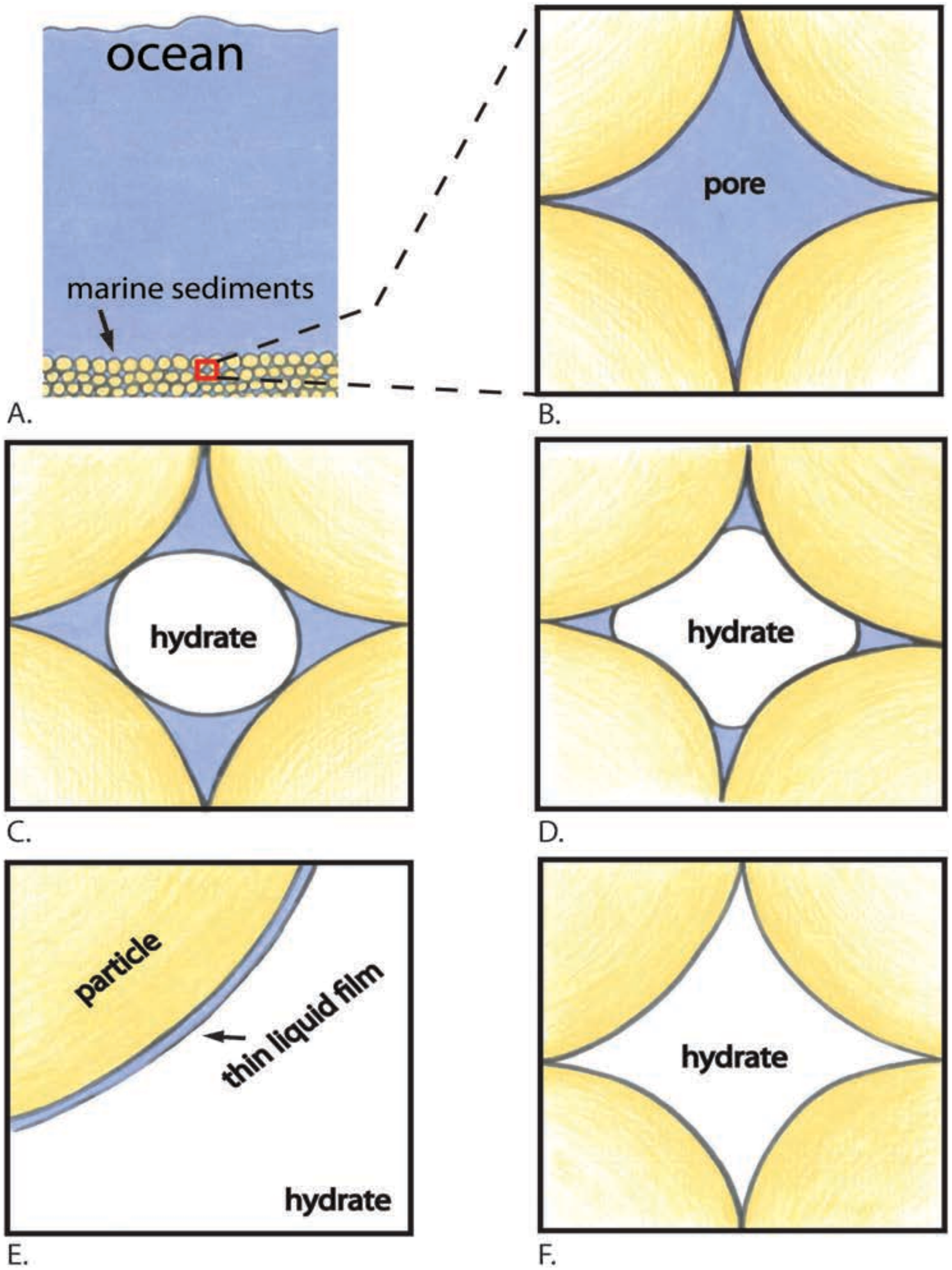

Fig. I.1. Diagram depicting the geometry of hydrate filling a pore. (A) Sedimentary particles at the seafloor. (B) An idealized view of the non-planar geometry introduced by particle contacts. (C) When liquid wets particle surfaces, the first hydrate crystal to form within a pore is approximately the shape of the largest sphere that will fit. (D) Continued hydrate growth proceeds by filling the crevices between particle contacts, leaving residual liquid pockets (blue) bounded by high hydrate-liquid interfacial curvatures. (E) Even far from bulk hydrate-liquid equilibrium, residual liquid pockets remains connected by thin liquid films that coat particle surfaces. (F) At very low temperatures the final residual liquid disappears.

The pore-scale effects we examine create small gas solubility differences between adjacent coarse and fine-grained sedimentary layers. Previous studies have associated the occurrence of hydrate anomalies (sharp increases in hydrate saturation) with the stratified arrangement of layers containing coarse particles sandwiched between layers containing finer particles (Clennell et al., 1999; Cook and Malinverno, 2013; Daigle and Dugan, 2011; Rempel, 2011). These gas hydrate anomalies are not simply controlled by the well-understood effects of temperature, pressure, and salinity on hydrate and liquid phase behavior. Instead the formation and behavior of these anomalies depend on the micro-scale effects and interactions between the ice-like hydrate and the intricate pore geometry dictated by the encompassing porous medium. Below, we quantify how the gas solubility changes as differences in particle-size distributions are encountered; this information can be used in reactive transport models for the evolution of gas hydrate deposits. We provide an example of this in **Section I.5,** where we predict the saturation of a hydrate anomaly given particle size distribution data and other input parameters required to characterize the site at which the hydrate was found (Rose et al., 2014). A generalized treatment that examines the relative contributions of permeability contrasts that produce flow focusing and the solubility contrasts that we focus upon here is the subject of **Section II.**

I.2. Theory

The changes in phase behavior produced by pore-scale effects can be conceptualized in terms of the undercooling ΔT, which is defined as the difference between the normal melting temperature of the solid that might be measured in a large laboratory vessel, and the observed melting temperature that pertains under confined conditions within the porous medium of interest. In hydrate-liquid systems, we are interested in how the disturbance to the phase equilibrium causes changes in the equilibrium solubility of methane dissolved in the aqueous solution adjacent to hydrate crystals. Once we determine the undercooling ΔT that is produced by pore-scale effects, we can calculate the modification to the equilibrium concentration as

$$c_{eq} \approx c_{bulk}\, exp(\frac{\Delta T}{\alpha}), \tag{1}$$

where c_{bulk} is the equilibrium concentration of the bulk solution neglecting porous medium effects at the *in situ* temperature and pressure, and the scaling temperature $\alpha = 14.4°\mathrm{C}$ for methane hydrate in salt-free water (Davie et al., 2004).

In **Section I.4**, we use laboratory data from ice-water and water-vapor systems to validate our modeling approach through comparisons against predicted changes in undercooling and matric potential. The process of predicting disturbances to the chemical potential in the ice-water and water-vapor systems is the same as predicting chemical potential disturbances in the hydrate-liquid system, for which there are comparatively few data. However, the shifts in chemical equilibrium in the ice-water and water-vapor systems, are typically measured in terms of the undercooling and matric potential, respectively, whereas we are interested in c_{eq}.

I.2.1. Phase Pressure Difference

Our focus is drawn to natural gas hydrate systems that aggregate over periods of centuries to millennia, allowing sufficient time to reach equilibrium phase distributions. We begin with a brief review of the well-understood ways that pore characteristics modify phase equilibrium. To build understanding, it is simplest to begin by considering a single component system that has two phases. Starting at a reference state with bulk melting temperature T_m and pressure P_m, equilibrium implies that

$$\mu_w(T_m, P_m) = \mu_{nw}(T_m, P_m), \tag{2}$$

where μ is the chemical potential, and the subscript w denotes a wetting phase variable, whereas nw denotes a non-wetting phase variable. The wetting phase against the sediment particles is assumed to be liquid water and the non-wetting phase will eventually be used to refer to hydrate, ice, or water vapor. Now we use the Gibbs-Duhem equation to write the following equalities describing the chemical potentials of the wetting and non-wetting phases in a perturbed state

$$\mu_w(T, P_w) = \mu_w(T_m, P_m) - s_w(T - T_m) + v_w(P_w - P_m), \tag{3}$$

and

$$\mu_{nw}(T, P_{nw}) = \mu_{nw}(T_m, P_m) - s_{nw}(T - T_m) + v_{nw}(P_{nw} - P_m), \tag{4}$$

where s is the specific entropy and v is the specific volume (Kofke, 1993; Lomba et al., 1996; Rempel et al., 2001) Equilibrium implies that we can equate the chemical potentials along the phase boundary, where T is the same in each phase but we allow the phase pressures to be different (i.e. $P_w \neq P_{nw}$) so that

$$0 = (-s_w + s_{nw})(T - T_m) + v_{nw}(P_w - P_{nw}) + (v_w - v_{nw})(P_w - P_m). \tag{5}$$

We introduce the latent heat L and densities ρ so that we can substitute

$$s_w - s_{nw} \approx \frac{L}{T_m}, \tag{6}$$

$$v_{nw} = \frac{1}{\rho_{nw}}, \tag{7}$$

and

$$v_w = \frac{1}{\rho_w} \tag{8}$$

to arrive at

$$0 = \frac{-L}{T_m}(T - T_m) - \frac{1}{\rho_{nw}}(P_{nw} - P_w) + \left(\frac{1}{\rho_w} - \frac{1}{\rho_{nw}}\right)(P_w - P_m). \tag{9}$$

To focus on the effects of the porous medium in modifying the phase behavior, we set the pressure in the wetting phase equal to the reference pressure P_m that defines the bulk melting temperature T_m and rearrange equation (9) to obtain

$$\frac{\rho_{nw}L}{T_m}(T_m - T) = \frac{\rho_{nw}L}{T_m}\Delta T = P_{nw} - P_w. \tag{10}$$

We can use equation (10) to calculate the perturbation that has occurred to phase equilibrium due to enhanced pressure in the non-wetting (i.e. solid) phase that arises from curvature and wetting effects.

I.2.2. Incorporation of Curvature Effects

First we consider the curvature effects. Laplace's equation (Laplace, 1831) implies that

$$\Delta P = P_{nw} - P_w = \gamma\kappa = \gamma\left(\frac{1}{r_1} + \frac{1}{r_2}\right). \tag{11}$$

Here, γ is the surface energy of the phase interface, κ is the curvature of the phase interface, and r_1 and r_2 are the principle radii of curvature along the phase interface. For a sphere $r_1 = r_2$, therefore across a spherical interface

$$\Delta P = \frac{2\gamma}{r}. \tag{12}$$

Equation (12) will be useful when the hydrate crystals can approximated as spheres, and also as a component of the calculation for the thin films that conform to the surfaces of the sediment particles, which we approximate as spheres.

I.2.3. Incorporation of Liquid Film

Next we account for the presence of thin liquid films that remain coated on particles far below the bulk melting temperature; this liquid is referred to in the literature as premelted films (Dash et al., 2006; Rempel et al., 2001). *Israelachvili* (2011) has exhaustively studied the details of wetting phenomena, but the thickness of liquid films are commonly described by a simple power-law equation (Cahn et al., 1992; Elbaum and Schick, 1995; Garvin and Udaykumar, 2006; Rempel and Worster, 1999; Tuller and Or, 2005; Watanabe and Mizoguchi, 2002). Other functional forms are possible, however, the qualitative behavior is always the same insofar as the film thickness must decrease as the pressure difference between the two phases is enhanced (Bischof et al., 1996; De Gennes, 1985; Hansen-Goos and Wettlaufer, 2010; Rempel et al., 2001). In this study, we account for wetting interactions using

$$\Delta P = P_0\left(\frac{\lambda_0}{d}\right)^{\beta}, \tag{13}$$

where β is controlled by the dominant microphysical interactions and is treated as constant, d is the thickness of the liquid film, and λ_0 is the film thickness at reference pressure P_0. By combining the wetting effects with the curvature effects from equation (11), we have the general relationship

$$\Delta P = \gamma\kappa + P_0\left(\frac{\lambda_0}{d}\right)^{\beta} = \gamma\left(\frac{1}{r_1} + \frac{1}{r_2}\right) + P_0\left(\frac{\lambda_0}{d}\right)^{\beta}, \tag{14}$$

which is the pressure jump across a curved interface separated by distance d from a particle surface. Now we can adapt this general relationship to describe the specific problem of wetting on the surface of a particle with radius R_p so that the two principle radii of curvature $r_1 = r_2 = -R_p$, which implies that

$$\Delta P = P_0\left(\frac{\lambda_0}{d}\right)^{\beta} - \frac{2\gamma}{R_p}. \tag{15}$$

Equation (15) is equivalent to the matric potential along the thin films that coat sediment particles in a liquid-vapor system. By substituting equation (15) into equation (10) we can describe the undercooling along a wetting film interface for an ice-liquid system, as

$$\frac{\rho_{nw}L}{T_m}\Delta T = P_0(\frac{\lambda_0}{d})^\beta - \frac{2\gamma}{R_p}. \quad (16)$$

For hydrates we are interested in the shift in solubility from the bulk equilibrium concentration c_{bulk}, to a new equilibrium concentration c_{eq}, because spatial variations in this shift in dissolved methane content help determine where hydrate anomalies form. Substituting equation (16) into equation (1), the equilibrium concentration can be described by

$$c_{eq} \approx c_{bulk}exp(\frac{\Delta T}{\alpha}) \approx c_{bulk}exp\left\{\frac{T_m}{\rho_{nw}L\alpha}\left[P_0\left(\frac{\lambda_0}{d}\right)^\beta - \frac{2\gamma}{R_p}\right]\right\}. \quad (17)$$

I.3. Methods

I.3.1. Modeling Pore Geometry

Rempel (2012) examined the effects of pore geometry on hydrate equilibrium using a two-dimensional packing of circular particles. We chose to adapt the problem to three dimensions because the pore geometry of three-dimensional sedimentary packing differs from two-dimensional pore geometry in two distinct ways. First, the pore itself is three-dimensional, therefore surfaces within three-dimensional pore have two principle radii of curvature rather than just one. Second, a difference in geometry arises from off-plane particle contacts in three-dimensional packing. We model three-dimensional pore geometry by simulating a sphere packing process in MATLAB (described in further detail in the **Section I.7**). To describe the geometry of the particle spheres that are being "packed," the model accepts as inputs a number of particles n, and either a Gaussian distribution with a mean radius r_{mean}, and standard deviation σ, or some other particle size distribution. This allows pore geometry to be simulated for a desired set of particles both when only an average value for the particle radii is available, as shown in *Section I.4.2-I.4.4*, and when an exact probability distribution for particle radii is available, as shown in **Section I.5**.

Once the packing process is complete, the three-dimensional pore geometry is available for evaluating the equilibrium phase perturbations. We implement a Monte Carlo integration routine in which the phase behavior is evaluated at a large number of randomly selected test points. If a given test point lands within a particle, the model records the event for a porosity calculation. If the test point falls within the pore space, we use the location of the test point and the geometrical constraints imposed by the nearest particles for a series of calculations to predict the magnitude of undercooling at which hydrate first encompasses that point. After the data are compiled, the residual liquid saturation is determined as the ratio of the number of test points that are outside the non-wetting phase at a particular undercooling relative to the total number of test points contained within the pore space.

I.3.2. Three-Dimensional Calculations

I.3.2.1. Pore Hydrate

As the temperature begins to drop below freezing, the curvature of the hydrate is primarily responsible for the undercooling, as illustrated in **Fig. I.2**. We calculate the largest sphere that can fit in the pore and still contain the test point, and refer to the resulting undercooling as the "pore hydrate" value.

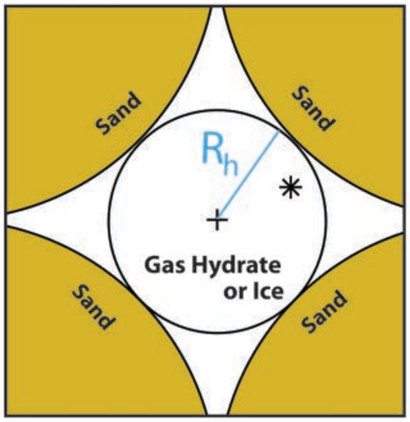

Fig. I.2. Simplification of pore hydrate geometry. The diagram shows how we use the location of a test point to find the radius R_h, of curvature for a pore hydrate. The asterisk is an example of a test point randomly chosen in a packing of spherical sedimentary or "sand" particles.

This process begins by first putting a sphere in the pore with the test point as the center and a radius that is equal to the distance between the test point and the nearest particle. Then we grow the sphere by incrementally moving its center point and changing its radius to match the new distance to its nearest neighbor. If the pore geometry does not permit a particular move or if the radius needs to decrease to avoid intersecting the particle, the model retains the previous size and location of the hydrate sphere. When the model reaches a set number of iterations, the radius is saved as the radius of the pore hydrate crystal R_h. The undercooling that would be required to place the point within this approximation for the largest hydrate crystal that could nucleate within the pore is found by combining equations (10) and (12) to obtain

$$T_m - T \approx \frac{T_m}{\rho_h L}\frac{2\gamma_{hl}}{R_h}. \tag{18}$$

I.3.2.2. Crevice Hydrate

After hydrate forms within a pore, the hydrate will continue to grow towards the particle contacts, as seen in **Fig. I.1D** and **Fig. I.3**. We simulate one of the principle radii of curvature of the "crevice hydrate" by finding the radius of the largest sphere that is tangent to the test point and the two particle spheres that are closest to the test point. The process of finding this radius involves several steps. First, the test point and the center points of the two nearest spheres are rotated into the same two-dimensional plane to solve for the radius of the largest tangent circle. The two nearest circles now have center points (x_1, y_1) and (x_2, y_2) and radii of r_1 and r_2, while (x_3, y_3) describes the location of the test point, with a radius of $r_3 = 0$. Apollonius, a Greek geometer with messianic tendencies from the 3rd century BC (Cantarella et al., 2002), showed that for any three initial circles, a total of eight tangent circles exists. However, by reducing one of the three initial circles to a point, the number of solution circles is reduced to two. The solution circles are tangent to the two initial circles and the two solution circles are tangent to the initial circle that has been reduced to a point. Because we want to solve for a tangent solution circle that has its center closer to the middle of the pore, only one of the solution circles is of interest, with its center at (x, y) and radius r. We find this solution by first using the equation of a circle to produce six quadratic equations, where $i = 1{:}3$, using

$$(x - x_i)^2 + (y - y_i)^2 - (r \pm r_i)^2 = 0. \tag{19}$$

Which can be expanded to six equations of the form

$$(x^2 + y^2 - r^2) - 2xx_i - 2yy_i \mp 2rr_i + (x_i^2 + y_i^2 - r_i^2) = 0. \tag{20}$$

By subtracting equation (20) with $i = 2$ from the version with $i = 1$, then repeating the procedure with $i = 3$ from $i = 1$, we obtain

$$ax + by + cr = d \tag{21}$$

and

$$a'x + b'y + c'r = d' \tag{22}$$

where

$$a = 2(x_1 - x_2), \quad a' = 2(x_1 - x_3), \tag{23 – 24}$$
$$b = 2(y_1 - y_2), \quad b' = 2(y_1 - y_3), \tag{25 – 26}$$
$$c = \pm r_1 \pm r_2\,, \quad c' = \pm r_1 \pm r_3, \tag{27}$$
$$d = (x_1^2 + y_1^2 - r_1^2) - (x_2^2 + y_2^2 - r_2^2), \tag{28}$$

and

$$d' = (x_1^2 + y_1^2 - r_1^2\,) - (x_3^2 + y_3^2 - r_3^2). \tag{29}$$

The equations above can then be substituted back into equation (19) and solved using the quadratic formula. For our purposes, the equations are simplified because $r_3 = 0$. Once we find the two Apollonius circles, the circles that are tangent to the test point and the two nearest circles, we can narrow down our solutions to the only circle that meets our requirements. Now we know the positive radius of curvature for the crevice hydrate, R_{h1}. In assigning the second principle radius of curvature, we consider two limiting cases. In the first, we approximate the crystal surface as locally spherical so that the second radius of curvature is the same. However, a second possibility presents itself in which the hydrate grows around the crevice in the third dimension. This scenario leads to a negative radius of curvature R_{h2} for the hydrate growing in the crevice points, as illustrated in **Fig. I.3**.

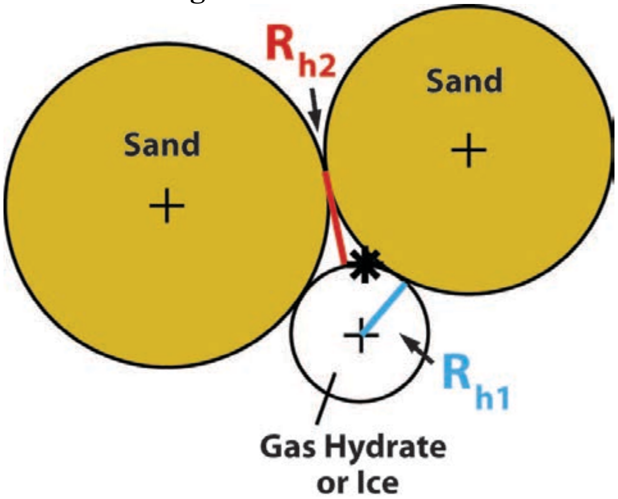

Fig. I.3. Simplification of crevice hydrate geometry. The diagram shows how we use a test point to find the positive and negative radii of curvature for a crevice hydrate, $R_{h1}$and R_{h2} respectively. The asterisk is an example of a test point randomly chosen in a packing of spherical sedimentary or "sand" particles.

Finally, we can calculate the perturbation to the chemical potential that would be required to place the point within a crevice between particles with a constant curvature hydrate-liquid interface using

$$T_m - T \approx \frac{T_m \gamma_{hl}}{\rho_h L}\left[\frac{1}{R_{h1}} - \frac{1}{R_{h2}}\right]. \tag{30}$$

I.3.2.3. Wetting Film

Even after hydrate saturates nearly all of the pore space, the particles are still coated by thin liquid films (**Fig. I.4**).

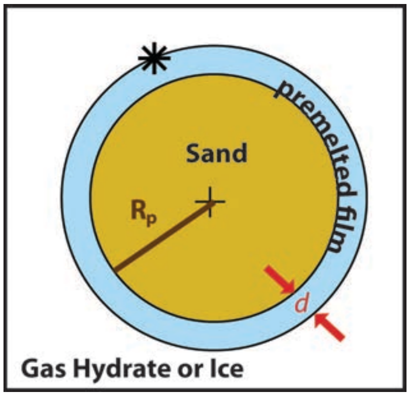

Fig. I.4. Simplification of liquid film geometry. The diagram shows how we use a test point to find the radius of curvature for a particle sphere nearest to the test point for the film undercooling calculation. The asterisk is an example of a test point randomly chosen in a packing of spherical sedimentary or "sand" particles.

We use the distance of the point from the particle d and the radius of the particle R_p to calculate the undercooling that would be required to place the point on the edge of a wetting film as

$$T_m - T \approx \frac{T_m}{\rho_h L}\left[P_0\left(\frac{\lambda}{d}\right)^{\beta} - \frac{2\gamma_{hl}}{R_p}\right]. \tag{31}$$

Equation (31) is essentially equation (16), with a more specific application to the hydrate-liquid system. The precise nature of the wetting interactions that produce liquid films depends on the surface chemistry and is the least well-constrained portion of our calculations. There exists a range of potential wetting interactions with different functional dependencies between undercooling and film thickness. To provide flexibility, we have produced a follow-up code that uses the geometrical output (i.e. R_{h1}, R_{h2}, d…) of the original model, but allows us to adjust any parameter, and the entire film thickness parameterization to test their effects.

I.3.3. Model Output

Equations (18), (30), and (31) yield estimates for the undercooling that is expected of "pore hydrate," "crevice hydrate," and "film hydrate." We use the largest of these perturbations to the melting temperature at each test point to determine the undercooling at that particular location. Once this process is completed for all of the desired test points, we can calculate the undercooling versus liquid saturation for the system. Here, the liquid saturation is defined as the fractional volume of the pore space that is occupied by liquid. Our model produces two total undercooling curves, which differ slightly in their treatments of "crevice hydrate", as noted above. In **Section I.4** and **Section I.5** we use both of the total curves from **Fig. I.5**, which we refer to as the "crevice curve" and the "pore curve", to fully test our model against analytical approximations and measured undercooling data. Later we show that the pore curve (Fig. I.5A) is more appropriate at higher liquid saturations and the crevice curve (Fig. I.5B) gains validity at lower liquid saturations.

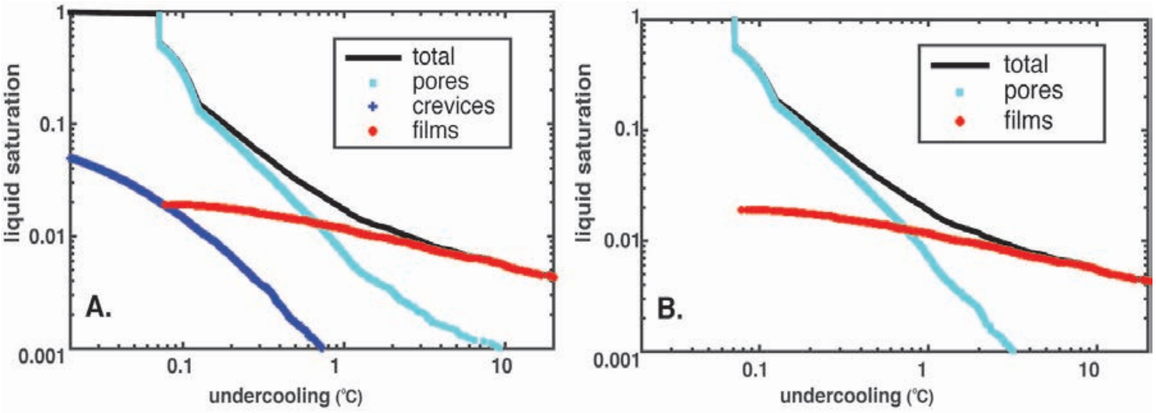

Fig. I.5. An example of model predictions. The black curves show the total predicted undercooling ΔT for a unit cube of simple-cubic packing with a radius, $r_{unit} = 1\mu m$. The portion of the total undercooling the model attributes to the initial occupation of pores by hydrate is plotted in cyan. The portion of the total undercooling the model attributes to hydrate that extends into crevices between particles is plotted in blue. The portion of the total undercooling that is caused the presence of thin liquid films is plotted in red. (A) Shows the undercooling curve that is influenced by the crevice hydrate points. Later we show that this curve, the crevice curve, becomes more valid at lower liquid saturations than (B). (B) Shows the undercooling curve that we refer to as the pore curve, in which the hydrate-liquid surface within crevices is approximated as spherical. Later we show that this curve is more valid at higher liquid saturations than the crevice curve.

For the crevice curve, we omit the pore hydrate calculation for test points that are in positions likely to be incorporated within crevice hydrates with two oppositely signed radii of curvature. This is judged by comparing the "particle-circle angle" subtended by line segments connecting the center of the Apollonius circle to the tangencies on two nearest particle spheres, to the maximum angle subtended by the line segments connecting the test point with the center of the Apollonius circle and each of the two tangencies. If this maximum angle is less than the "particle-circle angle," then the point is a candidate crevice point and we do not perform the pore-hydrate calculation for this point when we generate the crevice curve. In the second case, which we refer to as the pore curve, we omit this filtering step and treat each point as though it might fall on a hemispherical hydrate cap. Unfortunately, which of these two cases better represents the hydrate geometry at a particle test point depends on hydrate occupancy in adjacent pores and is not easily diagnosed by our numerical treatment. Nonetheless, we expect that the true saturation behavior will be somewhere between these limiting cases, and our calculations demonstrate that both sets of model saturation curves are similar (**Fig. I.5**).

The particle size distributions of the spheres we pack drastically affects the degree of undercooling i.e. the more fine-grained the particles, the more dramatic the undercooling or disturbance to the phase equilibrium. To illustrate this point, in **Fig. I.6** we plotted the undercooling curves for packed sphere models that have different mean radii r_{mean}, and standard deviation $\sigma = \frac{r_{mean}}{100}$. Notice that the slopes of the undercooling curves in log space begin to become more gradual at lower liquid saturations for the more fine-grained sphere packings; this is due to the increasing influence of the thin liquid films that coat the particles.

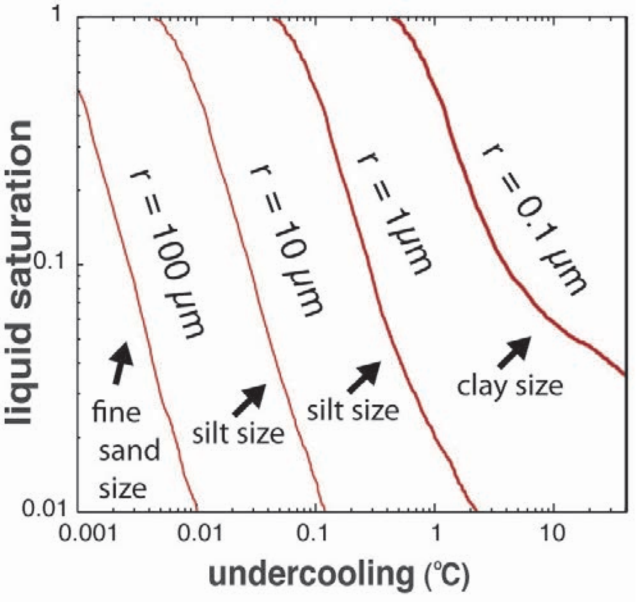

Fig. I.6. Particle size versus undercooling. This graph illustrates the change in undercooling magnitudes that accompany a change in mean radius, the smaller the mean radius, the larger the undercooling for a given liquid saturation. The mean radius is labeled as *r* on the graph. We only plot the pore total curve associated with each sphere packing to simplify the plot.

I.4. Model Validation

We test our model in several different ways. First we compare it against idealized simple-cubic (SC) sphere packing with an undercooling curve that has several attributes that are easily calculated analytically. Then we use our model to compare the model predicted undercooling against laboratory-measured values for two ice-liquid systems. Finally, we test our model by comparing the change in matric potential versus liquid saturation for a liquid-vapor system. The input parameters used by our model are described in **Table I.1**.

Table I.1. Model input parameters for the calculations that are discussed below.

	Idealized Packing	Ice-liquid	Ice-liquid	Liquid Vapor
Composition of porous medium	None – computationally modeled sphere[1]	Polystyrene powder[1]	Graphitized carbon black powder[1]	Millville Silt Loam[2]
$\boldsymbol{r_{mean}\ (\mu m)}$ mean radius	1[1]	2.5[1]	0.1075[1]	17.1[2]
$\boldsymbol{\sigma\ (\mu m)}$ standard deviation	0[1]	0.16*	0.0625[1]	0.385*
$\boldsymbol{T_m\ (K)}$ reference temperature	273[1]	273[1]	273[1]	273[1]
$\boldsymbol{\rho\ \left(\frac{kg}{m^3}\right)}$ density non-wetting phase	917[1]	917[1]	917[1]	NA
$\boldsymbol{\gamma\ \left(\frac{J}{m^2}\right)}$ interfacial surface energy	0.029[1]	0.029[1]	0.029[1]	0.073[3]
$\boldsymbol{L\ \left(\frac{J}{kg}\right)}$ latent heat	917[1]	917[1]	917[1]	NA
$\boldsymbol{\lambda_0\ (\mu m)}$ film thickness at p_0	3.5e-9[1]	3.5e-9[1]	3.5e-9[1]	1.6e-6
$\boldsymbol{p_0\ (Pa)}$ scale for disjoining pressure	1.1e6[1]	1.1e6[1]	1.1e6[1]	1.1e6[1]
$\boldsymbol{\beta}$ power-law exponent for film thickness	3[1]	3[1]	3[1]	3[1]

NA is not applicable

[1] Source is *Cahn et al.* (1992)

[2] Estimated using values provided in *Or and Tuller* (1999)

[3] Source is *Vargaftik et al.,* (1993)

*Not provided; we used $\boldsymbol{\sigma = \sqrt{r_{mean}/100}}$.

I.4.1. Comparison to Analytical Approximation

We compare our undercooling predictions for idealized SC packing against an analytical approximation for idealized SC packing (**Fig. I.7**).

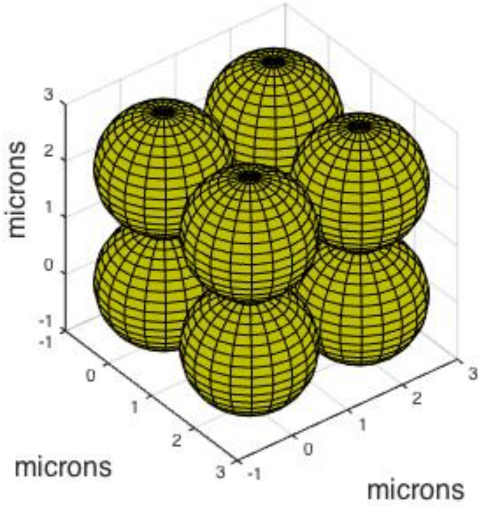

Fig. I.7. An example of simple-cubic packing of spheres with radii $r_{sc} = 1\mu m$ shown at an oblique angle.

Cahn et al. 1992 use the geometry of SC sphere packing to predict the evolution of ice formation as a function of undercooling within an idealized pore space. They develop theoretical equations for the undercooling of ice freezing in SC sphere packing for any given radius that we refer to as, r_{sc} (Cahn et al., 1992). We modify the equations used to develop their theoretical curve to match only the undercooling effects that we account for in this study, by neglecting grain-boundary effects that are sensitive to unknown crystallinity.

In **Fig. I.8** we illustrate some important features of the undercooling predictions produced by our model. Notice that the pore total curve does a better job matching the expected behavior from a liquid saturation of 1 to about 0.35 than the crevice total curve. This suggests that the pore total undercooling curve is more accurate at warmer temperatures than the crevice total curve. The crevice total curve does a better job matching the expected behavior starting around a liquid saturation of 0.1 and below. This suggests that while erroneous at warmer temperatures, the crevice total undercooling curve becomes more accurate as the temperature continues to drop and the liquid saturation decreases. Further calculations suggest neither of the model predicted curves accurately captures the undercooling between the liquid saturations of about 0.35 to about 0.1 for SC sphere packing. However, the similarity between the two models and the analytical approximation suggests that the resulting errors in predicted saturation are likely small.

We expect this difference between the pore and crevice undercooling curves because the hydrate surface is locally spherical as solid first begins to fill the pore space, whereas saddle-shaped surfaces gain in importance as the solid continues to fill the pore space and the temperature decreases (**Fig. I.1**). Both of the predicted undercooling curves converge as the temperature continues to drop and wetting interactions between the solid, liquid, and particles begin to dominate over curvature effects. We use both curves in our model comparisons against laboratory data in *Section I.4.2*.

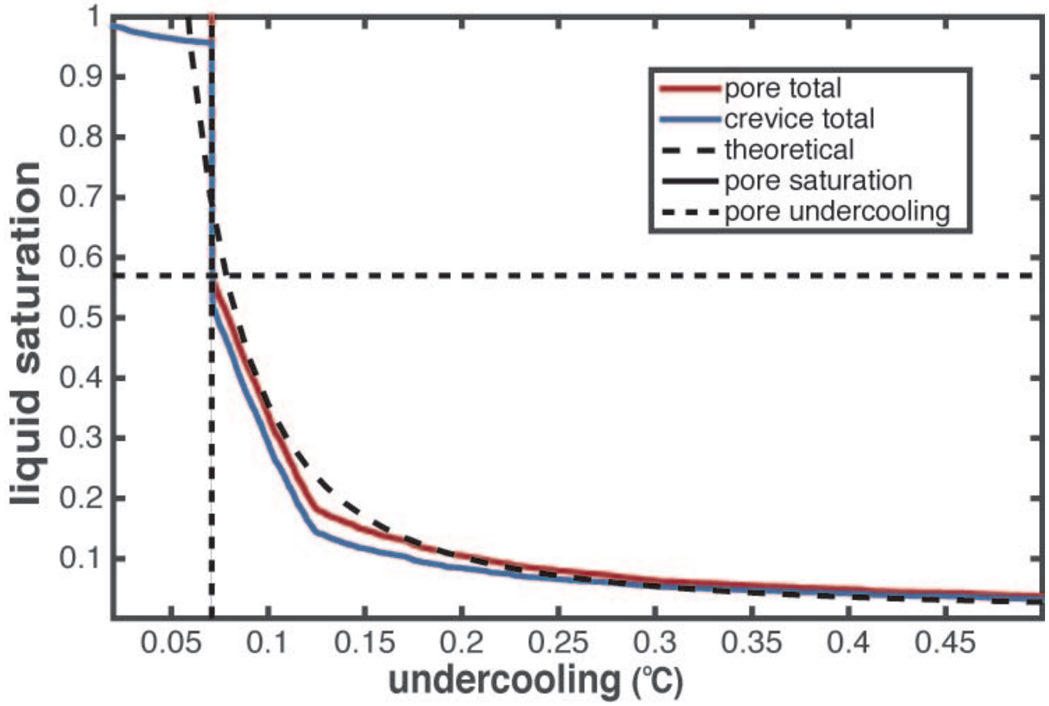

Fig. I.8. Model predicted undercoolings versus analytical approximations. The figure contains both the model predicted pore total undercooling curve, shown in red, and the model predicted crevice total undercooling curve, shown in blue. The black dashed curve is the analytical approximation from *Cahn et al.* (1992) that approximates the undercooling based on the geometry of SC sphere packing with a radius of $r_{sc} = 1\mu m$ accounting for crevice and film points, but not the pore hydrate points included in this study. The dashed straight lines intersect at the first kink in our model's curves. This kink occurs at a liquid saturation of 0.57, and undercooling 0.078 °C, that correlate to the central pore being filled by the largest sphere that can occupy the void space. The pore total curve captures this feature, but the crevice total curve allows hydrate formation at warmer temperatures than are possible, a limitation also shared by the *Cahn et al.* (1992) approximation.

I.4.2. Ice-water Comparisons

After the successful comparison between our model predictions and anticipated behavior in simple-cubic packing, we compare our model results to laboratory data as shown in **Fig. I.9**. We use two undercooling datasets from *Cahn et al.* (1992) for a two-phase ice-water system within a medium composed of monosized spheres composed of polystyrene powder and graphitized carbon black. First we compare our model results against the measured undercooling values for the graphitized carbon black (**Fig. I.9A**).

When comparing our model's undercooling predictions against the undercooling data for graphitized carbon black powder, **Fig. I.9A**, both curves fit entirety of the dataset well. However, at saturations above approximately 10%, the pore total slightly overestimates the undercooling liquid. This is not surprising because the pore total curve should account for an excess of curvature effects, leading to slightly over-predicted undercooling values.

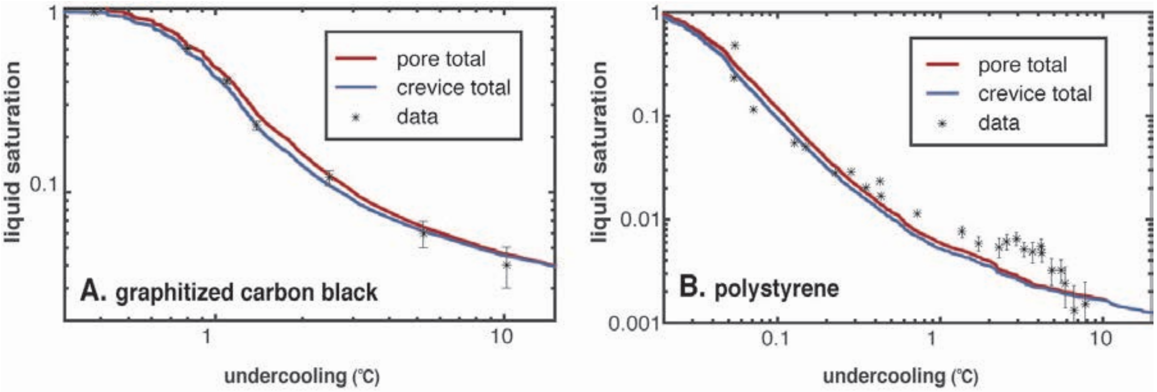

Fig. I.9. Model predicted undercooling versus undercooling data from ice melting laboratory experiments. The red curves in both plots represent the undercooling curves that are dominated solely by pore ice until the liquid saturation is sufficiently low for the wetting effects to govern. The blue curves in both plots represent the undercooling curves that are influenced by crevice ice. Notice that the axes are slightly different between the plots, optimized for the data that each is displaying. (A) Comparison of our model's undercooling predictions against undercooling data for ice melting in mono-dispersed graphitized carbon black powder shown in black asterisks (Cahn et al., 1992). The R-squared values for the pore and crevice curves in (A) are 99.35% and 99.75%, respectively. (B) Comparison of our model's undercooling against undercooling data for ice melting in mono-dispersed polystyrene powder shown in black asterisks (Cahn et al., 1992). The R-squared values for the pore and crevice curves in (B) are 82.33% and 79.25% respectively.

When comparing our model's undercooling predictions against the undercooling data for the polystyrene powder, both curves mimic the general trend of the data, but the model does not do nearly as good of a job predicting the undercooling in **Fig. I.9B** as it does for graphitized carbon black in **Fig. I.9A**. However, notice that in **Fig. I.9A**, only two of the data points fall below 10% liquid saturation. In **Fig. I.9B**, the majority of the data occurs between 10% and 0.1% liquid saturation. At such low liquid saturations, wetting effects are responsible for most of the residual liquid. The detailed nature of the intermolecular forces that cause premelted films to form is the least well-constrained part of our calculation. In fact, because wetting effects are dependent on particle composition and surface chemistry, we expect some variance in the undercooling effects between the two systems depicted in **Fig. I.9A** and **Fig. I.9B**. Due to the complicated nature of the premelted films, we developed our model to output the predicted undercooling data as well as geometrical information we compiled for pore characteristics that could affect hydrate growth at each test point. This allows us to run quick simulations where we can recalculate the undercooling curve for the same pore geometry but with desired adjustments in the reference film thickness λ_0, the power-law exponent β, or any of the other input parameters. This is useful for undercooling values such as those shown in **Fig. I.9B**, where several of the data points occur where the liquid saturation is between 1% and 0.1% and the behavior of pre-melted films can become increasingly complex (Cahn et al. 1992). Although we treat the reference film thickness and power-law exponent as poorly constrained, and hence, "free" parameters, it is worth emphasizing that wetting effects are unimportant at high liquid saturations and the impressive agreement between data and predictions in this regime does not depend on any adjustable parameters.

I.4.3. Liquid-vapor comparison

The adsorption of water to sedimentary particles in a liquid-gas system occurs in the vadose zone. This important effect is essential for plants to obtain water in unsaturated soil, and is a consequence of the same physical effects (wetting interactions and surface energy) that cause undercooling in ice-liquid systems. We compare our model prediction for the matric potential of Millville silt-loam against experimental results (Or and Hanks, 1992; Or and Tuller, 1999; Tuller and Or, 2005) in **Fig. I.10**.

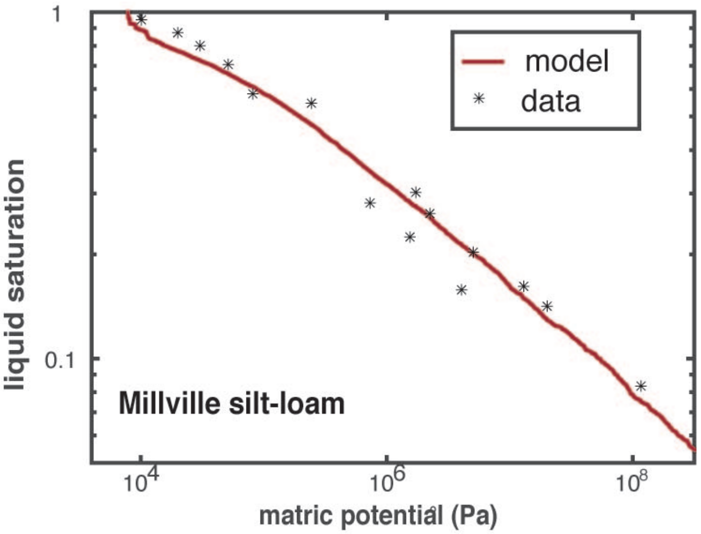

Fig. I.10. Model predicted matric potential curve versus matric potential data. This plot displays the comparison of our model's prediction plotted as a red curve to data from *Or and Hanks's* (1992) laboratory experiments plotted as black asterisks. Notice that the slope of the curve is more gradual than those in **Fig. I.9**. This shallow slope of the matric potential curve for this dataset suggests that wetting effects are dominating the system. To match the data we require strong intermolecular forces, so we increase λ_0 in comparison with the previously used values (**Table I.1**). Because wetting effects dominate, the pore total curve and the crevice total curve are nearly identical and we only plot the pore total curve. The model predicted curve accurately predicts the matric potential required for the saturation to begin decreasing. The R-squared value for our matric potential curve is 96.84%.

The λ_0 parameter, which scales the film thickness, needed to match the data was nearly three orders of magnitude larger than the λ_0 used for the ice-liquid experiments (**Table I.1**). It is not entirely unexpected that the Millville silt-loam sediments might produce stronger wetting effects than the powders used in *Section I.4.2*. The most obvious difference is that natural soil with a significant clay content was used by *Or and Hanks* (1992). The intermolecular forces active in natural soil may cause wetting effects to be stronger or weaker than in laboratory prepared monosized powders (Saarenketo, 1998). The Millville silt-loam sediments are composed of a broad range of particle sizes: 33% sand, 49% silt, and 18% clay (Or and Tuller, 1999). To estimate the mean radius r_{mean}, we used estimates on the finer side of their particle size classifications for each grain size, where radius of sand particles = $50\mu m$, radius of silt particles = 1 μm, and radius of clay particles = 0.5 μm. Because loam is composed partly of clay, the surface wetting interactions are likely even more complex (Oss and Giese, 1995). The presence of clay in the Millville silt loam presents another issue, inherent to the sphere-packing model design: non-spherical particles. The presence of non-spherical particles likely has a dramatic effect on the ability of our code to model the pore geometry accurately, thereby affecting our ability to predict disturbances to the chemical potential caused by the pore geometry. If the average of the specific surface areas ($76.5\text{m}^2/\text{g}$) reported in *Or and Tuller*

(2005) for the Millville silt loam is used to calculate a spherical particle radius using a silica density of $2.65 \mathrm{g/cm}^3$, the corresponding radius should be about 0.015 μm, which is about three orders magnitude smaller than our estimated radius shown in the table at 17.1 μm. As the size of spherical particles decrease, their specific surface area increases linearly; the relationship between clay particles and specific surface area is not as simple. However, by simply increasing λ_0 we have been able to produce model results that well approximate the data.

I.5. Discussion and Applications

Our model is designed so that particle size distributions from adjacent layers can be used to predict the phase behavior that leads to the growth of hydrate anomalies. The particle size distribution data allow us to predict the equilibrium concentration difference between adjacent sedimentary layers. This is important because the methane concentration at layer boundaries is tied to the equilibrium concentration in the coarser material in which hydrate precipitates, as illustrated in **Fig. I.11** (Clennell et al., 1999; Cook and Malinverno, 2013; Daigle and Dugan, 2011; Rempel, 2011).

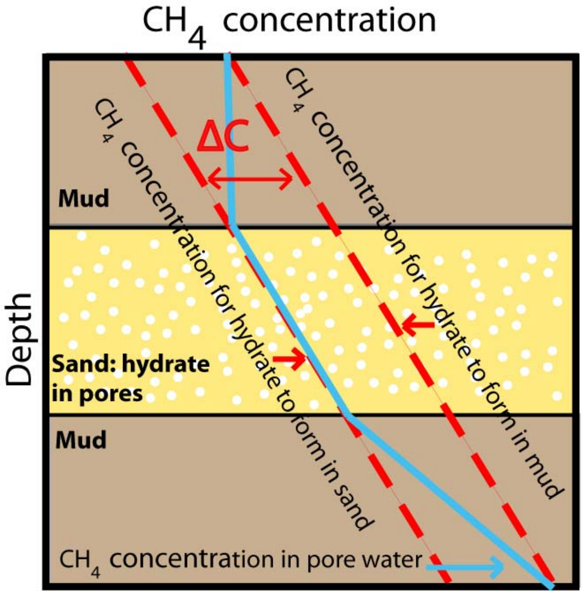

Fig. I.11. Layer boundary effects on methane concentration, modified from **Figure I.4** in *Cook and Malinverno 2013*. This diagram illustrates that although there is a jump in equilibrium concentration of methane between the mud and the sand (red dashed lines), the concentration of methane within the pore water cannot abruptly change (light blue line). Therefore, in the locations where the mud is directly adjacent to the hydrate-bearing sand, methane hydrate is absent in the mud (Cook and Malinverno, 2013).

To demonstrate how our model could be used to predict hydrate anomalies using particle size distributions, we use borehole data collected during the Indian National Gas Hydrate Program Expedition 1 (NGHP-01) at site 17A in the Andaman accretionary wedge (Collett et al., 2008; Rose et al., 2014). Here, thin (~10 cm), coarser-grained ash layers punctuate the stratigraphic record, which is otherwise dominated by pelagic sediments (Rose et al., 2014). These ash layers contain anomalous accumulations of hydrate, in many cases filling more than 70% of the ash pore-space (Rose et al., 2014). Such hydrate saturation anomalies may be the result of diffusive methane flux from finer-grained sediments into coarser-grained layers (Cook and Malinverno, 2013; Malinverno and Goldberg, 2015; Rempel, 2011). Using our model, we predict undercooling values for the ash and pelagic sediment layers at NGHP-01 site 17A given particle size distributions for each layer from *Rose et al.* (2014).

First, we use the plot from **Figure I.3** from *Rose et al.,* (2014) describing the ash layer and the surrounding bulk sediments from core 51X to calculate the probability distribution functions (PDFs) for the particle radii. We use these PDFs to create two sets of randomly ordered spheres (**Fig. I.12**).

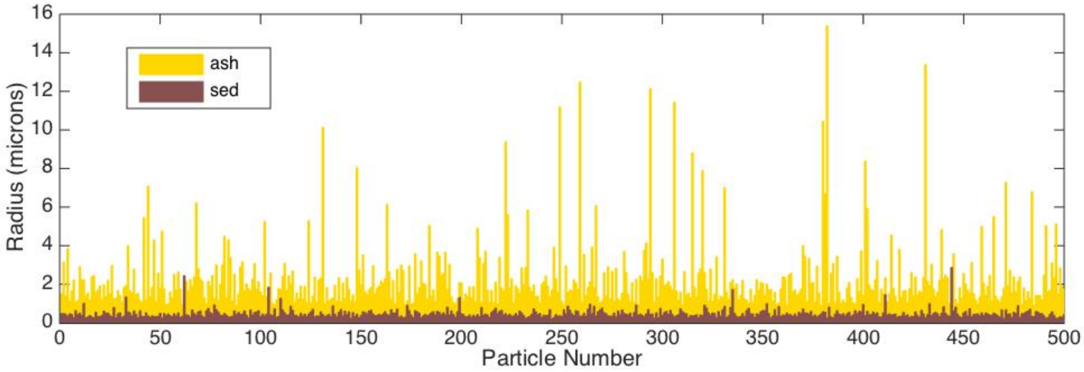

Fig. I.12. Randomized radii distribution for the first 500 particles for layers created by using the data from **Figure I.3** in *Rose et al., 2014*. Notice that the ash particles are substantially coarser than the bulk sediments that encompass the ash layer.

Once the datasets describing the particle sizes have been randomized, we were able to pack the spheres and mimic the pore space geometry of the ash and surrounding bulk sedimentary layers (**Section I.7**). We use the methods outlined in **Section I.3** to predict the undercooling for each of the datasets (**Fig. I.13**).

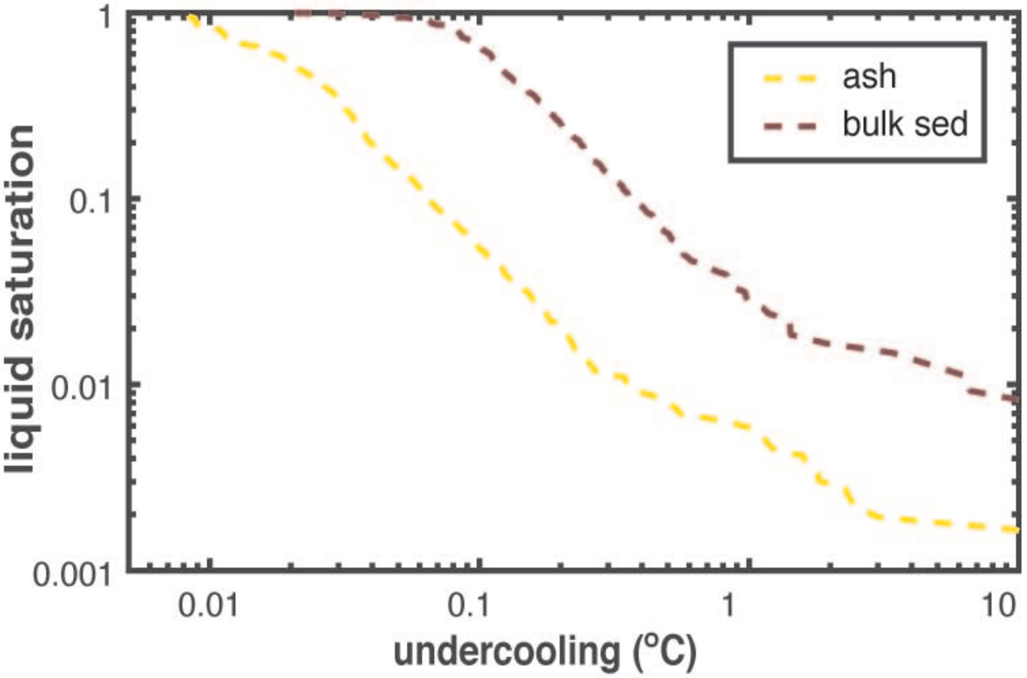

Fig. I.13. Undercooling curves for hydrate model. This plot shows that as hydrate forms and the liquid saturation reduces, the undercooling caused by the pore geometry and interactions with the particles more dramatically affects the finer grained sediments relative to the coarser ash layers. This implies that at the same subzero temperature, more hydrate will be frozen in the coarser ash layer than in the more fine-grained sedimentary deposits layer.

However, for hydrate anomalies, we are interested in how porous media affect the solubility of methane in aqueous solution adjacent to the hydrate within each layer. By utilizing equation (17), we convert the undercooling caused by the porous medium to the change in equilibrium concentration relative to the bulk equilibrium concentration (**Fig. I.14**).

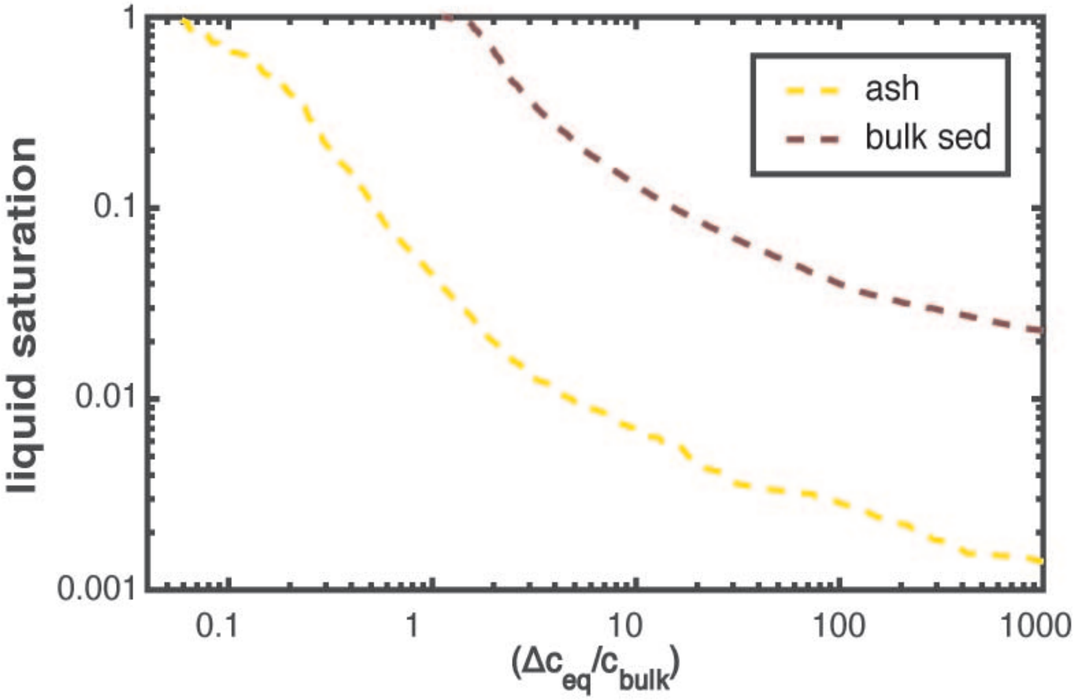

Fig. I.14. Relative porous medium effects on equilibrium concentration. This plot shows that the difference in equilibrium concentration required for hydrate freezing within a porous medium is greater in the more fine-grained sedimentary layer. This difference in equilibrium concentrations causes methane hydrate solubility differences between the adjacent layers that are ultimately the cause of hydrate anomalies. Because the altered equilibrium concentration in the more fine-grained sedimentary layer is higher than in the ash layer, hydrate is slightly more stable in the coarser ash layer (Cook and Malinverno, 2013; Rempel, 2011; Malinverno and Goldberg, 2015). Therefore, the higher concentration of methane required for hydrate to form in the adjacent fine-grained deposits cannot be achieved until sufficiently high hydrate saturation (corresponding with a liquid saturation of a few percent in this figure) is reached in the ash layer.

The difference in solubility between the adjacent layers is an important factor when considering hydrate anomaly formation (Rempel, 2011). By using our tools described in this paper, we can predict this difference in solubility. In **Fig. I.15** we show the results of a model that used our model's results as input along with parameters provided in *Rose et al.,* (2014) to predict the saturation of methane hydrate growing within the ash layer sandwiched between more fine-grained sediments.

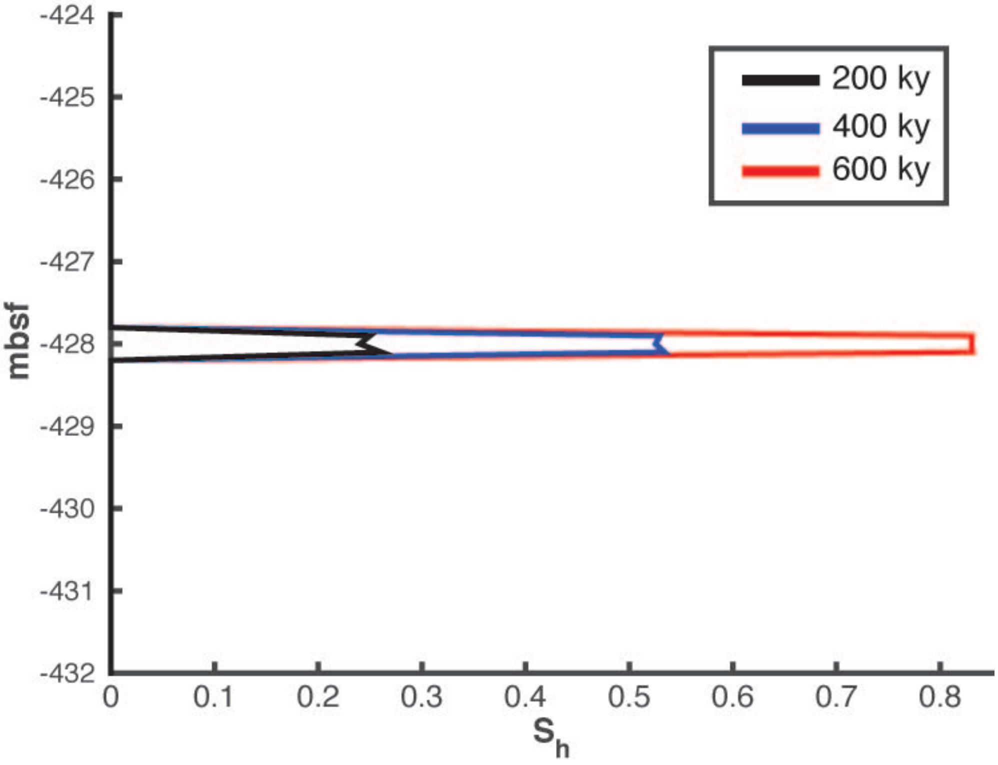

Fig. I.15. Hydrate saturation over time. This plot shows the hydrate saturation S_h versus meters below seafloor (mbsf) predicted using parameters from *Rose, et al.* (2014) and the model predicted differences in undercooling. The model predicted hydrate saturation of the anomaly is 80.7% and measured hydrate saturation of the anomaly is 83%. The different colored lines correspond to how long the hydrate was allowed to accumulate in the model. This figure was provided by Brandon VanderBeek.

Following the 1D formulation of *Rempel* (2011), we use the predicted undercooling curves from the model to predict the diffusive growth of hydrate within a horizontal, 10 cm thick ash layer at 428 meters below the seafloor (Rose et al., 2014). For modeling simplicity, we approximate the dependence of undercooling on hydrate saturation as a power-law relationship and find the best-fit exponent ($\beta = 1.35$) to the undercooling curves in **Fig. I.13** for liquid saturations between 0.02 and 0.75. This approach is valid as we are interested in hydrate saturations well below 98%. We assume dissolved methane is supplied from below at an upward fluid transport rate of 0.5 mm/a, a rate representative of the region (Dewangan et al., 2011) and the pore water methane concentration is initially at equilibrium. Additional site-specific information required to model hydrate accumulation includes water depth (1344 m), seafloor temperature (5.5 °C), geothermal gradient (0.021 °C /m), and depth to the base of the gas-hydrate stability zone (605 mbsf) are taken from *Rose et al.* (2014). We find hydrate saturations reach 83% within the thin ash layer at 600 ka (**Fig. I.15**). The sediment surrounding the ash layer contains <1% hydrate. These results compare well with borehole measurements at NGHP-01 site 17A, where a 9.5 cm thick ash layer at 428 mbsf was found to contain 81% hydrate (Rose et al. 2014). However, because the age of the hydrate deposit is unknown, similar hydrate saturations can be produced for a range of undercooling values. Nonetheless, pore-scale effects control the size and distribution of hydrate anomalies and will continue to prove useful when characterizing hydrate reservoirs.

I.6. Conclusions

As we continue to increase our understanding of the nature and distribution of gas hydrates, we become more aware of the importance of gas hydrate anomalies. In an effort to help predict the occurrence and saturation of gas hydrate anomalies, we focus our efforts on understanding the pore-scale effects that are likely to be the cause of the gas hydrate anomalies (Rempel, 2011; Rose et al., 2014; **Section II**). The differences in sedimentary properties, particularly grain size, between adjacent sedimentary layers produce small differences in the equilibrium concentrations. These small differences contribute towards the generation of gas hydrate anomalies that are particularly important for slope-stability considerations (**Section III**) and may even contain most of the volume of gas hydrate off the continental shelf (Clennell et al., 1999; Cook and Malinverno, 2013; Daigle and Dugan, 2011; Rempel, 2011). We demonstrate that our tool closely approximates the chemical disturbance to the equilibrium within porous media that have mostly spherical particles. Our model is less effective at capturing the pore geometries of sedimentary layers that contain non-equant particles and the associated increase in the importance of wetting interactions within these layers. However, the increase in the strength of the wetting interactions is attributed to the increase in specific surface area of clay particles. This suggests that scaling expected film thickness by the ratio of specific surface areas in the modeled spherical and actual non-equant cases might prove a viable strategy to account for enhanced wetting effects. Indeed, our comparison in *Section I.4.3* demonstrates the potential of such an approach. These predictions are a useful first step towards developing reliable, quantitative interpretations for the conditions that determine observed hydrate content and distribution in natural reservoirs.

I.7 Appendix: Modeling a 3D Porous Medium

We created a tool that simulates a sphere packing process in MATLAB to use the curvature of the spheres and the void space geometry between the spheres as a way to model the pore space geometry of naturally accumulated sediments. As stated in *Section I.3.1*, the model can run given inputs as straightforward as the number of desired particles n, a mean radius value r_{mean}, and standard deviation σ. However, the tool can also create a data set for a set of n particles from a particle size distribution curve, or even from a volume percent versus radius curve; the latter was developed for the specific application addressed in **Section I.5**. We cover the steps for the sphere packing process started by inputting a particle size distribution to determine the distribution of particle radii (**Fig. I.16**), as the overall sphere packing process is the same regardless of the chosen input.

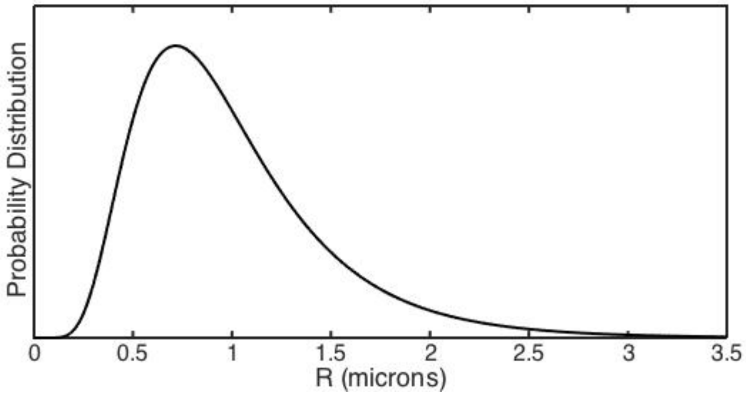

Fig. I.16. A probability distribution function (PDF) for the radii of a set of particle spheres. This particular PDF describes a set of particles with $r_{mean} = 1\mu m$ and $\sigma = 0.5\mu m$ for a set of $n = 1000$ particles.

To create a set of particles whose radii satisfy the PDF in **Fig. I.16**, we must sum the probabilities for each radius of the PDF to calculate the corresponding cumulative distribution function (CDF) as shown in **Fig. I.17**. We can then split the CDF into n equal intervals, each n division corresponds to a particle radius r.

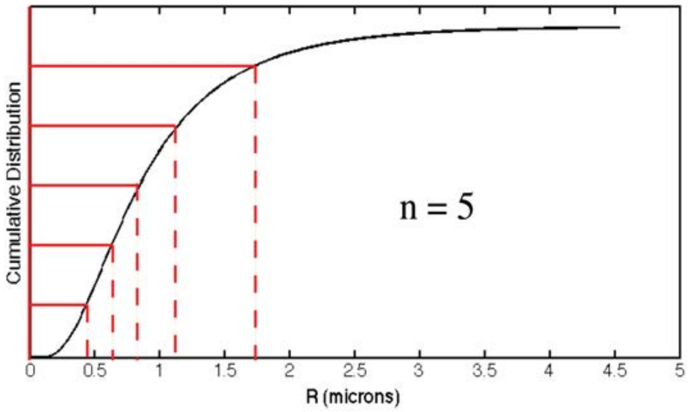

Fig. I.17. The segmentation of a cumulative distribution function to create a dataset containing particles with radii that satisfy a corresponding PDF. Here, n is chosen to be 5 for the purpose of illustrating the process used to choose the radii. The solid red lines show equally spaced probability of n intervals. For each probability interval, there is a corresponding radius, illustrated by the dashed red lines. For n intervals we determine n radii.

After the CDF has been used to choose n particle radii, we have a synthetic data set that describes the radii of n particles (**Fig. I.18**).

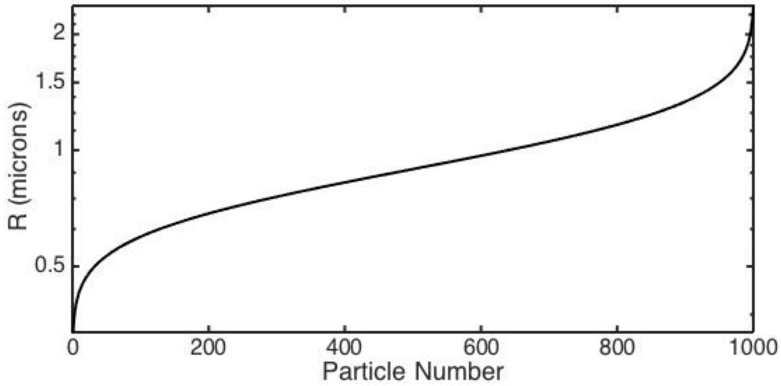

Fig. I.18. Particle spheres with their corresponding radii. In this plot $n = 1000$.

Once a set of n particles has been developed that satisfy the desired PDF, our next step is to randomize the order of the particles (**Fig. I.19**). We randomize the particle order because our sphere packing process involves dropping the particle spheres one by one and the goal is to create a pore geometry with natural characteristics.

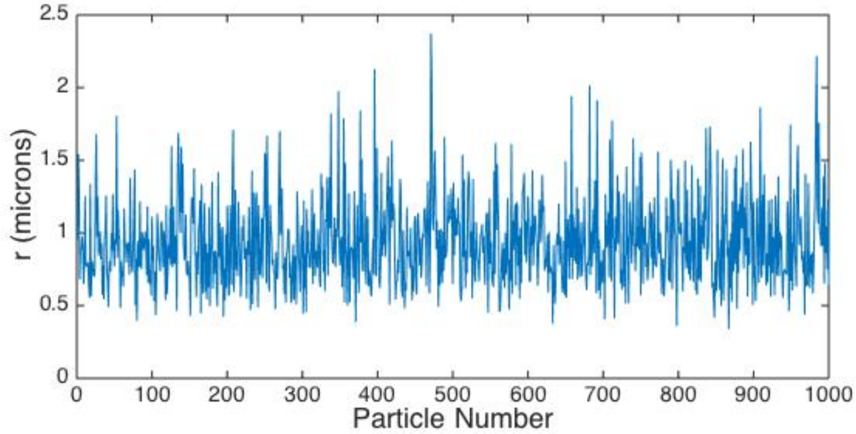

Fig. I.19. Randomized particle spheres and their corresponding radii. In this plot $n = 1000$.

Once the dataset containing the randomized particle spheres is complete, we can begin the sphere dropping process. The process works by dropping each particle sphere one at a time. We simulate the dropping process by first choosing an arbitrarily high z-coordinate. Then the x-y coordinates at which each particle sphere is dropped is chosen by first defining lengths of a "container" and randomly choosing x-y coordinates within the specified x-y container space. The particle sphere is then "dropped" down the z-axis with the corresponding x-y coordinates. We mimic this process by checking the x-y position of all of the previously dropped spheres to see if the dropping sphere and the previous spheres would overlap. If there are no previously dropped spheres within this "window," then the particle sphere will make contact with the "ground" defined at $z = 0$ (**Fig. I.20A**). If the dropped sphere comes into contact with a previously dropped sphere, it begins to roll longitudinally off of the sphere, we mimic this process by decreasing the angle between the center of the previously dropped sphere and the center of the dropping sphere (**Fig. I.20B**). If the dropped sphere does not come into contact with a second dropped previously sphere as it is "rolling" around the previously dropped sphere, then it is dropped and the dropping process is repeated but with a new x-y "window." If the dropped sphere does come into contact with a second previously dropped sphere, it becomes tangent with both of the previously dropped spheres (**Fig. I.20C**). At this point, the "fitting" process begins. The fitting process involves the dropped sphere going through a series of very small lateral and longitudinal rotations until the dropped sphere also becomes tangent to the floor or a third previously dropped sphere.

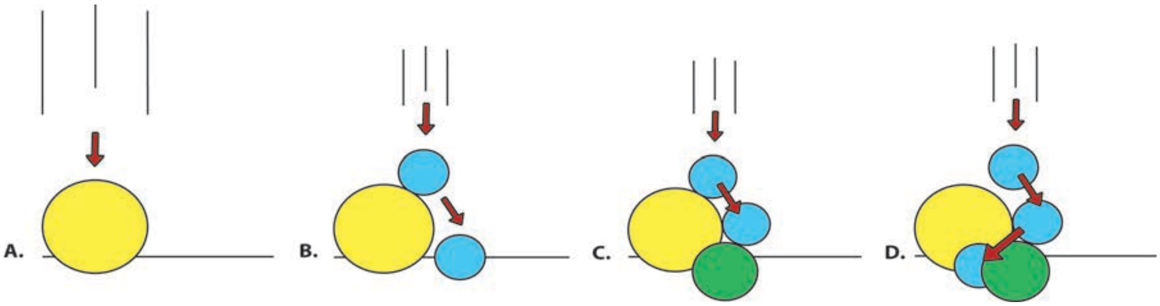

Fig. I.20. A simplification of the sphere packing process. In this diagram the colored circles are used to represent particle spheres. (A) The yellow sphere drops to the floor at z = 0 and does not contact another sphere on its way down. (B) The blue sphere is dropped and makes contact with the yellow sphere. The blue sphere rolls tangentially around the yellow sphere until it is again dropped and then makes contact with the floor. (C) The blue sphere is dropped and again make contact with the yellow sphere. This time, as the blue sphere rolls tangentially down the yellow sphere, it makes contact with a second previously dropped sphere. The dropped blue sphere becomes tangent to both the yellow and the green sphere. (D) After the blue sphere becomes tangent to both the yellow and green spheres (C), the blue sphere will repeat a number of rotations that allow the dropped blue sphere to roll downwards while maintaining its tangencies to the two initially contacted spheres.

A sample of the results of such a sphere packing process is shown in **Fig. I.21**. The dropping, rolling, and fitting processes are intended to create a sphere packing that is more natural than an idealized packing, with the additional benefit of not having to explicitly characterize the geometry of each pore within the sphere packing.

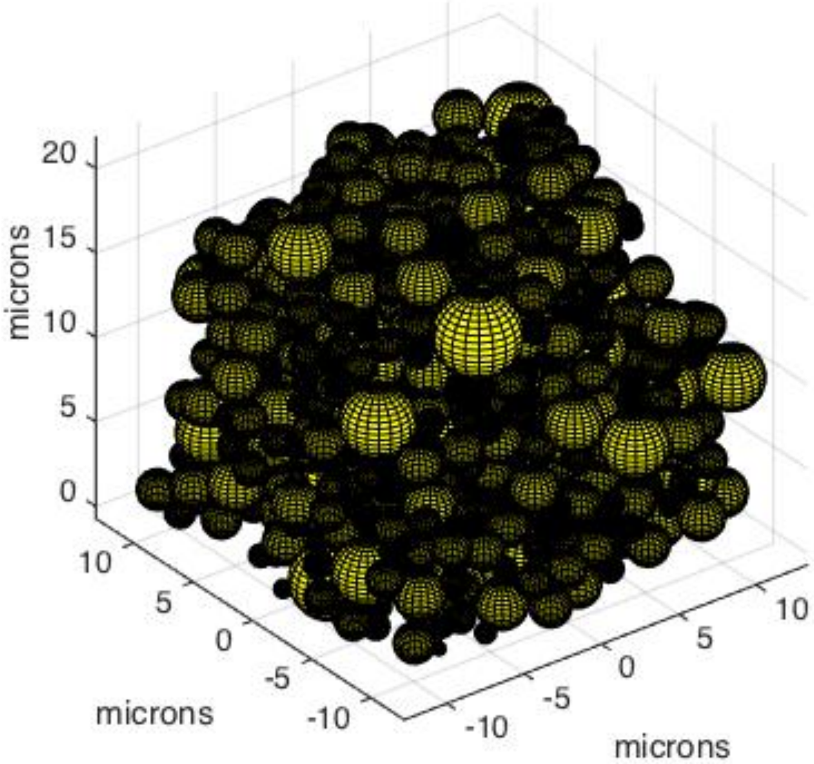

Fig. I.21. An example packing of spheres with $r_{mean} = 1\mu m$ and $\sigma = 0.5\mu m$ for a set of $n = 1000$ particles, which have radii that satisfy the PDF in **Fig. I.16**. A cross-section at a chosen height can then be taken from the packing of heterogeneously sized spheres and used for testing. Much larger packings can be made, but this size of an assemblage is appropriate for displaying the results of the sphere packing process.

II. Pore-scale controls on the distribution of hydrate in marine sediments

This section concerns the origins of anomalies in hydrate distribution that are commonly found near transitions in sediment grain size, in part due to the phase equilibrium perturbations discussed in **Section I**. This portion of our study constituted part of the PhD research conducted by University of Oregon graduate student, Brandon VanderBeek; a modified version of this section will soon be submitted for publication a peer-reviewed journal as"On the importance of flow-focusing and diffusive transport in controlling the distribution of methane hydrate in marine sediments", by Brandon P. VanderBeek and Alan W. Rempel

II.1. Introduction

The ubiquity of methane-hydrates stored within the sediments of Earth's continental margins has made these substances of broad scientific interest. Marine methane-hydrates play an important role in the global carbon cycle (*Kvenvolden*, 1993; *Dickens et al*., 1997; *Judd et al*., 2002). They pose a geologic hazard as sources for matrix instabilities that may lead to slope failures (see **Section III**) and large volumes of methane release to the atmosphere (*Maslin et al*., 2004; *Sultan et al.*, 2004). Lastly, production of methane from hydrate deposits may supply future energy needs (*Kvenvolden*, 1993). Quantifying the formation rates and spatial distribution of naturally occurring hydrates is critical to the investigation of these issues.

The physical processes that control the bulk characteristics of hydrate reservoirs are captured reasonably well by long-established model formulations (*Rempel and Buffett*, 1997; *Davie and Buffett*, 2001) that are rooted in laboratory-verified phase equilibrium parameterizations (*Duan et al*., 1992; *Zatsepina and Buffett*, 1997; 1998) and field-based estimates of in situ conditions (*Riedel et al*., 2006). However, detailed geophysical investigation of numerous hydrate systems has shown that the spatial distribution of hydrate is strongly heterogeneous and often correlates with the physical properties of the host sediments (*Torres et al*., 2008; *Bahk et al*., 2013; *Rose et al*., 2014). Anomalously high hydrate saturations (volume fraction of pore space filled by hydrate) found in association with relatively more coarse-grained strata have been attributed to both enhanced fluid focusing through more permeable sediment layers (e.g., *Weinberger and Brown*, 2006; *Boswell*, 2009) and to perturbations in phase equilibrium related to pore-space geometry (*Torres et al*., 2008; *Malinverno*, 2010; *Rempel*, 2011). In order to understand the conditions under which known hydrate accumulations formed and to achieve more accurate predictions of hydrate occurrence, the influence of pore architecture on growth dynamics must be incorporated into modeling efforts. In this letter, we demonstrate how pore-size effects on methane solubility and permeability-driven variations in fluid flux can be parameterized into a 1D model for hydrate growth along dipping, coarse-grained layers imbedded in a finer-grained sediment package. Our modeling shows that sharp gradients in methane solubility, which occur along stratigraphic boundaries, promote the growth of localized regions of high hydrate saturation while enhanced fluid advection favors more distributed growth throughout high permeability layers. The framework we develop holds promise for using observations of hydrate distribution within anomalous deposits, together with measured sediment properties to infer pore fluid advection rates and formation time scales during reservoir emplacement.

II. 2. Model

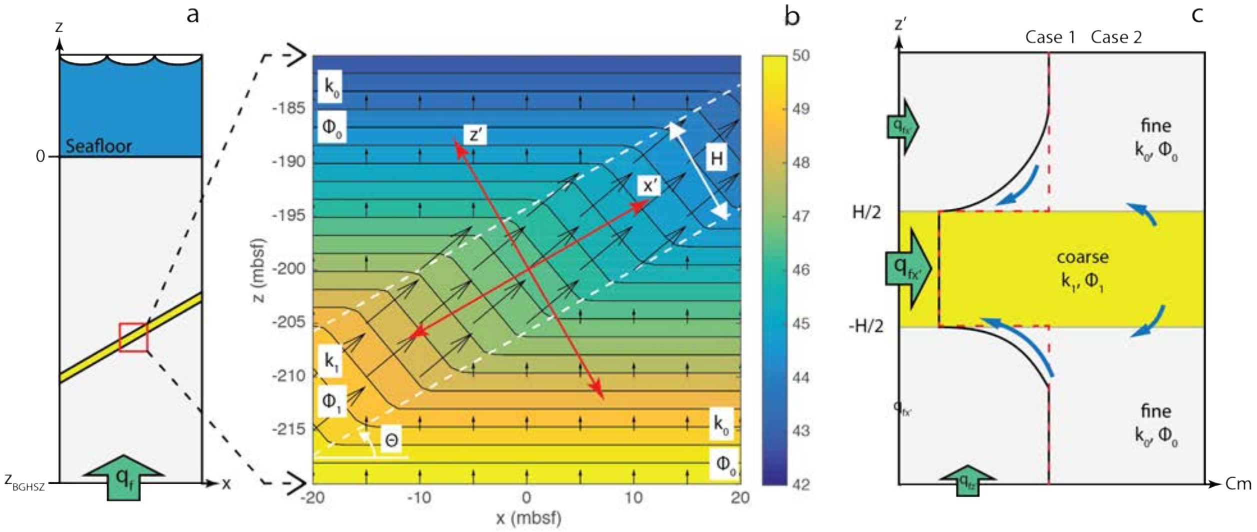

Figure II.1. Model domain and methane transportation mechanisms. (a) Schematic depiction of the model domain (red box) showing a dipping permeable layer (yellow region) surrounded by sediments less amenable to fluid transport. Methane is transported into the model in the dissolved phase (green arrow) from a deep source region. (b) The flow field surrounding the more permeable layer (outlined in white) and associated non-hydrostatic pressure gradient required to drive flow is shown. The x'- and z'-axes that define our model domain are drawn in red. Model parameters discussed in text are shown. (c) Methane transportation mechanisms in our model. Methane is advectively supplied in the layer-normal (z') and layer-parallel (x') directions (green arrows with larger arrow indicating greater advective methane flux). The dashed red lines schematically depict the methane solubility in the fine-(grey region) and coarse-grained (yellow region) sediments at low hydrate saturations (Case 1) and when the hydrate saturation in the more permeable layer is substantially greater than that in the fine-grained sediments (Case 2). The solid black lines illustrate the methane saturation profiles for Case 1 and 2. In Case 1, the reduced methane solubility within the coarse-grained layer results in an enhanced diffusive flux of methane (blue arrows) from the fine-grained sediments into the coarse-grained sediments. In Case 2, high hydrate saturations within the permeable layer promote diffusive transport of methane out of the coarse-grained sediments.

II.2.1 Conceptual model

To asses the importance of pore architecture on influencing methane transport processes and hydrate distribution, we model a small (~10 meter) region within the GHSZ containing a dipping coarse-grained layer (e.g., a fault or sand-rich unit) that is more amenable to fluid transport than the surrounding finer-grained sediments (Fig. II.1a). Methane is supplied in the dissolved phase via the vertical advection of pore fluids originating from a deeper methane source region. The permeable layer provides a conduit for enhanced fluid flow (Fig. II.1b), which results in more rapid accumulation of hydrate in comparison with that in the surrounding sediments. Pore geometry perturbs two-phase thermodynamic equilibrium between methane in hydrate and methane in solution by requiring interstitial hydrate to attain high surface curvatures (*Clennell et al*., 1999; *Henry et al*., 1999) and also as a result of the wetting interactions that cause thin liquid films to intervene between particle and hydrate surfaces (*Rempel*, 2011; **Section I**). As a result, the concentration of methane in solution at local equilibrium is greater in the finer-grained sediments, where pore sizes are smaller, compared to the coarse-grained layer (Fig II.1c; Case 1). Consequently, methane accumulation is further enhanced within the layer through chemical diffusion. The occlusion of pore space by hydrate effectively reduces the pore size. As hydrate accumulates more rapidly in the coarse-grained layer, the associated increase in equilibrium methane concentration reduces the diffusive flux of methane into the layer. At high hydrate saturations, the equilibrium methane concentration may even be perturbed enough such that methane is diffusively transported out of the layer (Fig. II.1c; Case 2).

II.2.2 Mass balance equation and flow focusing

We solve a single mass balance equation for methane assuming methane is only present dissolved within the pore water or as hydrate. We write our conservation equation as

$$\varphi\rho_h[X_m - C_m(1 - X_m)]\frac{\partial S_h}{\partial t} + \varphi\rho_l(1 - S_h)\frac{\partial C_m}{\partial t} = \\ -\rho_l\vec{u}_{z'}\cdot\nabla C_m + D\rho_l\nabla\cdot[(1 - S_h)\nabla C_m] + S_m\ , \tag{1}$$

where C_m and X_m are the mass fractions of methane in water and hydrate, respectively; S_h is the volume fraction of the pore-space occupied by hydrate; ρ_l and ρ_h are the densities of the pore fluid and hydrate, respectively; φ is the sediment porosity; $\vec{u}_{z'}$ is the prescribed layer-normal Darcy transport velocity; D is the intrinsic dispersivity of methane in solution and t is time. The last term, S_m, is a source term that accounts for the layer-parallel, advective and diffusive methane fluxes (discussed below). We assume methane is only transported in the dissolved phase and local sources are negligible (i.e., biogenic production).

To account for the effects of flow focusing in our 1D model, we approximate a dipping sediment layer as a laterally extensive sheet. Similar to waves, porous flow is refracted upon passing through an interface defined by a change in permeability (*Middleton and Wilcock*, 1994). Conservation of mass requires the flux of pore fluid in the layer-normal direction to be constant while the flux in the layer-parallel direction is proportional to the ratio of the layer and background permeabilities. We write the x'- (layer-parallel) and z'-components (layer-normal) of the Darcy transport velocity as:

$$u_{z'} = \vec{u}\frac{\varphi_0}{\varphi_1}\cos\theta\ , \tag{2a}$$

$$u_{x'} = \vec{u}\frac{k_1\varphi_0}{k_0\varphi_1}\sin\theta\ , \tag{2b}$$

where $\vec{u}$ is the prescribed vertical Darcy transport velocity at the base of the modeling domain and θ is the layer dip angle measured from the horizontal direction (Fig. II.1b). The permeability, k, and porosity, φ, vary in the z'-direction and take on values of k_0 and φ_0 (the background permeability and porosity) or k_1 and φ_1 (the permeability and porosity within the layer). Provided our modeling domain is located a significant distance away from the termination of the dipping layer, this simple treatment of flow focusing should provide a good approximation. Indeed, comparison of this approximation with more complex 2D flow modeling (*Chatterjee et al.*, 2014) shows this to be true. The far-field flux into the base of the model is assumed everywhere to be constant. Reductions in permeability are expected as hydrate fills the pore space (e.g., *Kleinberg et al.*, 2003). However, because significant along-dip spatial variations are expected to be accommodated over length scales that are much larger than the layer thickness, our 1D treatment is an appropriate simplification. In order to focus upon the essential behavior, for simplicity we assume that the layer-normal and layer-parallel fluid fluxes remain constant in time regardless of variations in hydrate saturation.

II.2.3 Thermodynamic considerations

Two-phase thermodynamic equilibrium between methane in hydrate and in solution is primarily a function of temperature, pressure, and the concentration of additional solutes (notably salt in marine settings). Within the hydrate stability zone, *Davie et al.*, (2004) show that the concentration of methane at equilibrium C_{eq} is well approximated by an exponential function of temperature T, namely

$$C_{eq} \approx (1 - \zeta C_s) C_3 \exp\left(\frac{T - T_3}{\alpha}\right), \tag{3}$$

where C_3 is the three-phase equilibrium methane solubility at the base of the gas-hydrate stability zone (BGHSZ; this value is determined from a linear function of temperature and pressure; see eq. 3 in *Davie et al.*, 2004); T_3 is the temperature at the BHSZ; C_s is the concentration of dissolved salts; α and ζ are theoretically determined constants with values 14.4 °C and 0.1 mol^{-1}, respectively.

In porous media, the large curvature, and correspondingly high surface energy, of the hydrate-liquid interface contributes significantly to the Gibbs free energy of the system (*Clennell et al.*, 1999; *Henry et al.*, 1999). This results in a depression of the hydrate freezing point (henceforth referred to as undercooling) and increase in methane solubility that is not accounted for in eq. 3. The undercooling (ΔT_f) at which hydrate first forms is inversely proportional to the radius of curvature of the largest crystal that will form within the pore space, so that

$$\Delta T_f \approx \frac{2\gamma_{hl} T_m}{\rho_h \mathcal{L} R}, \tag{4}$$

where γ_{hl} is the surface energy of the hydrate-liquid interface; T_m is the local bulk melting temperature; $\mathcal{L}$ is the latent heat of fusion; and R is the pore radius. Increased hydrate saturation reduces the available pore space and increases the effective undercooling. This behavior is captured well with a power-law relationship in which the intrinsic undercooling is increased by a factor of $(1 - S_h)^{-1/\beta}$ where the exponent depends on the architecture of the pore space; here we adopt $\beta = 1.3$ (*Rempel*, 2011). At high hydrate saturations ($S_h > 95\%$), the physics of thin liquid films that separate interstitial hydrate from the pore walls cause deviation from this single power-law behavior (*Rempel*, 2011). For this reason, all simulations are terminated before S_h exceeds 95%. This does not significantly limit our model's applicability, as most natural hydrate systems, including those containing notable hydrate saturation anomalies (e.g. *Rose et al.*, 2014), do not exceed this threshold. Recently, *Irizarry and Rempel* (2015) developed a more advanced model for determining the intrinsic undercooling of host sediments and the dependence on hydrate saturation given a particle-size distribution. In general, the results of *Irizarry and Rempel* (2015; see also **Section I**) confirm the power-law relationship proposed by *Rempel* (2011) and so we use the simpler formulation defined above. Following *Rempel* (2011), eq. 3 can be modified as follows to account for the effects of simple pore geometries and hydrate growth on equilibrium methane solubility,

$$C_{eq} \approx (1 - \zeta C_s) C_3 \exp\left[\frac{T - T_3}{\alpha} + \frac{\Delta T_f}{\alpha (1 - S_h)^{1/\beta}}\right]. \tag{5}$$

II.2.4 Modeling procedure and assumptions

Hydrate growth is modeled according to eq. 1, which is discretized to second-order in space and integrated through time using MATLAB's® implicit ODE solvers. We track the accumulation of methane in solution and in hydrate at each model node; the accumulating phase is determined from eq. 5 (i.e. hydrate forms where the methane concentration exceeds the two-phase solubility). We prescribe the background, vertical Darcy transport velocity and the undercooling for the layer and surrounding sediments. Given the sediment undercooling values and assuming the host sediment grain radius (r_g) is comparable to the pore radius, the well-known relation $k = cr_g^2$ (*Krumbein and Monk*, 1943) with equation 4 is used to estimate the permeability contrast between the layer and background sediments:

$$\frac{k_1}{k_0} = \left(\frac{\Delta T_{f0}}{\Delta T_{f1}}\right)^2 . \tag{6}$$

Equation 6 is then used to derive the layer-parallel fluid velocity (eq. 2b). By assuming this relationship between grain size and permeability, we limit our parameter space to two primary variables, the vertical Darcy transport velocity and each layer's undercooling. These values values may be estimated from routine geophysical measurements and core samples. For example, flowmeter measurements (e.g. *Tryon et al.*, 2002), borehole temperature data (e.g. *Torres et al.*, 2004), and heat flow measurements (e.g. *Davis et al.*, 1990) may be used to derive vertical fluid advection rates. Using eq. 5, sediment undercooling can be estimated from the mean grain radius as determined from the particle-size analyses of sediment cores (e.g. *Torres et al.*, 2008; *Rose et al.*, 2014). We use the imposed background fluid velocity to derive a steady-state advective thermal profile that is imposed in our model. In order to estimate the layer parallel methane fluxes (S_m in eq. 1), we assume that the initial methane concentration is poised at bulk equilibrium (eq. 3) in all our simulations. Gradients in methane solubility in the x'-direction are primarily driven by changes in temperature, as neither S_h nor ΔT_f is expected to vary significantly in this direction. We define the methane flux in the x'-direction as

$$S_m = -\vec{u}_{x'}\rho_l \frac{\partial C_{eq}}{\partial T(x')} + D\rho_l(1 - S_h)\frac{\partial^2 C_{eq}}{\partial T(x')^2}. \tag{7}$$

.

To emphasize the effects of pore architecture on the distribution of hydrate we make the following assumptions (in addition to those previously mentioned). (1) Hydrate formation proceeds rapidly enough relative to the rates of methane supply that the kinetic effects on equilibrium can be ignored; this assumption is supported by experimentally determined rates of hydrate formation (*Rehder et al.*, 2002; *Zatsepina and Buffett*, 2003). (2) Salinity and temperature perturbations associated with the latent heat of hydrate formation and the occlusion of salt from the hydrate lattice, respectively, may be ignored; this assumption is valid provided the rate at which thermal and salinity perturbations are advectively and diffusively removed is much greater than the rate of hydrate accumulation. (3) Hydrate formation is not limited by water availability (i.e. the pore spaces remain water-saturated). (4) We neglect the effects of sedimentation and compaction, as well as the potential for perturbations to the particle packing that result from interactions with the growing hydrate.

II.3. Results

Parameter	Value	Units	Description
$\boldsymbol{C_m}$	--	--	Mass fraction methane in water
$\boldsymbol{X_m}$	0.134	--	Mass fraction methane in hydrate
$\boldsymbol{S_h}$	--	--	Hydrate saturation of pore space
$\boldsymbol{\rho_l}$	1029	kg/m^3	Seawater density
$\boldsymbol{\rho_h}$	930	kg/m^3	Hydrate density
$\boldsymbol{D}$	10^{-9}	m^2/s	Intrinsic dispersivity of methane in solution
$\vec{\boldsymbol{u}}$	1	cm/a	Vertical Darcy transport velocity
$\boldsymbol{\theta}$	--	°	Layer dip
$\boldsymbol{k_0}$	--	m^2	Background permeability
$\boldsymbol{k_1}$	--	m^2	Layer permeability
$\boldsymbol{\varphi_0}$	0.5	--	Background porosity
$\boldsymbol{\varphi_1}$	0.5	--	Layer porosity
C_3	2.3e-3	--	Mass fraction methane at the BGSZ
T_3	19	°C	Temperature at the BGHSZ
$\boldsymbol{\alpha}$	14.4	°C	Methane solubility constant from Davie *et al*., 2004
$\boldsymbol{\zeta}$	0.1	mol^{-1}	Salt solubility constant from Davie *et al*., 2004
$\boldsymbol{\gamma_{hl}}$	0.035	J/m^2	Hydrate-liquid surface energy
C_s	0.035	--	Mass fraction salt in solution
$\boldsymbol{\mathcal{L}}$	430	kJ/kg	Latent heat of fusion
$\boldsymbol{\beta}$	1.3	--	Undercooling exponent [Rempel, 2011]
$\Delta \boldsymbol{T_f}$	--	°C	Undercooling

Table II.1 Nominal parameter values and associated descriptions. Where not specified here, values used are given in the text.

II.3.1 Hydrate growth in heterogeneous sediments

To illustrate the effects of pore architecture on hydrate formation, we consider the accumulation of hydrate in a 4 m thick layer dipping 60° from horizontal. The center of the layer is located at 200 m beneath the seafloor (mbsf). We prescribe a vertical fluid velocity of 10 mm/a and an advective temperature profile assuming a seafloor temperature of 4 °C (at 2000 m water depth) and a temperature of 19 °C at the BGHSZ (at 250 mbsf). These conditions are similar to those identified along the northern Cascadia margin (IODP Site 311) (*Riedel et al*., 2006). We assume a constant pore water salinity of 3.5% by weight, constant sediment porosity of 50%, and a fine-grained sediment undercooling of 0.01 °C (consistent with a grain radius of ~5 µm, which is similar to the mean grain size observed in silty clay layers of turbidite deposits at IODP Site 311 *Torres et al*., 2008). We use a node spacing of 10 cm, which previous scaling analysis of our governing equation (*Rempel*, 2011) suggests is sufficient to resolve the spatial variations in hydrate saturation described below. Table II.1 lists the variables, descriptions, and values used in our modeling.

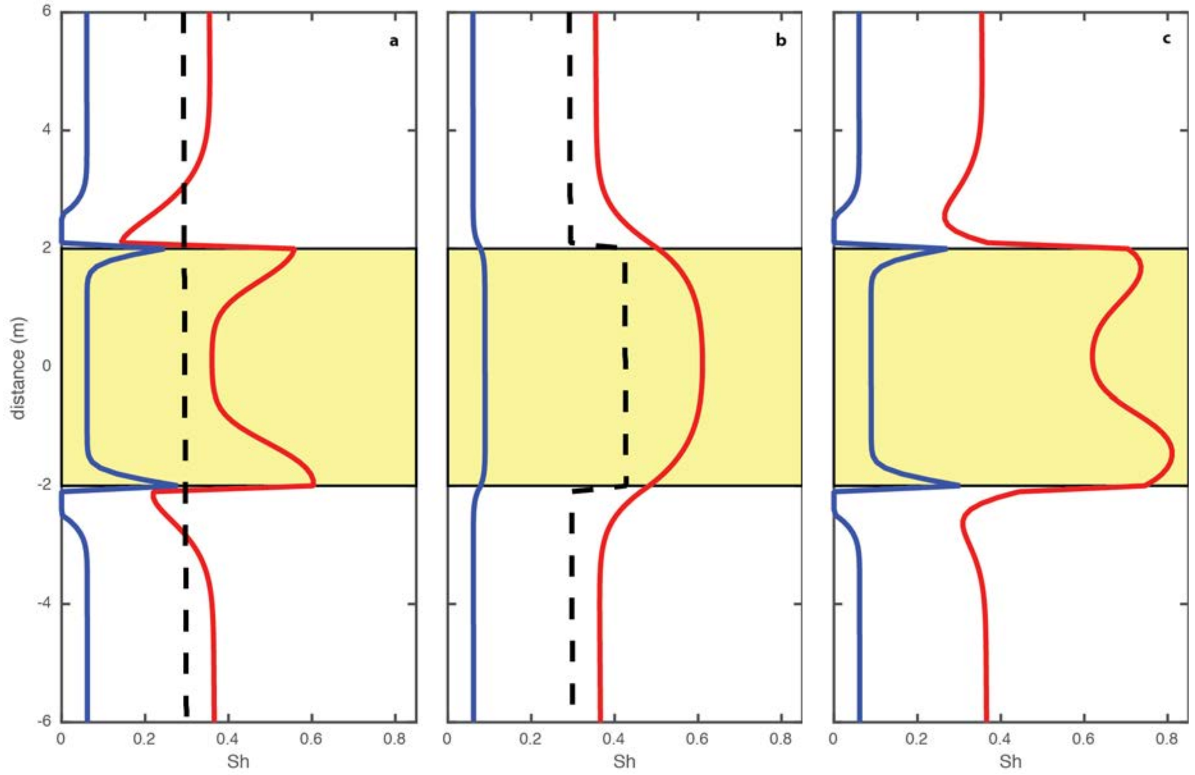

Figure II.2. Hydrate saturation profiles for fine- and coarse-grained undercooling values of 0.01 °C and 0.005 °C (representing a factor of 2 change in pore size). Solutions are drawn at model output times of 50 kya (blue line) and 200 kya (red line). The white and yellow backgrounds identify fine- and coarse-grained regions, respectively. The dashed black lines show hydrate saturation at 200 kya without accounting for pore size effects on methane solubility. (a) Hydrate saturation profiles neglecting enhanced advective flux through the more permeable layer. (b) Hydrate saturation profiles neglecting the influence of intrinsic pore size on methane solubility. (c) The predicted hydrate saturations accounting for both pore size and permeability variations.

We first examine the effects of pore size on hydrate growth, neglecting the influence of enhanced fluid flow (Fig. II.2a). We prescribe an undercooling of 0.005 °C to the layer and allow methane to accumulate for 200 kya. Away from stratigraphic boundaries hydrate forms slowly in concert with previous 1D models (e.g. *Rempel and Buffett*, 1997) and the sediment undercooling has a negligible effect. At the stratigraphic boundary, the equilibrium methane solubility is greater within the fine-grained sediments than within the coarse-grained sediments. Continuity in methane concentration at this boundary requires an undersaturated zone to exist in the adjacent fine-grained sediments (Fig. II.1c; Case 1), which we refer to as the hydrate-free region (HFR) (see *Rempel*, 2011). Within the coarse-grained layer a prominent 'spike' in S_h develops. This hydrate spike is a consequence of an enhanced diffusive flux of methane driven by the abrupt change in equilibrium conditions at the layer boundary. With increased time the width of the HFR shrinks while the width and amplitude of the hydrate spikes grow. In Fig. II.2b, we show the influence of enhanced fluid flow through the more permeable layer while neglecting intrinsic variations in sediment pore size (the influence of S_h on the equilibrium methane concentration is included). The contrast in particle size across the layer boundary results in a modest factor of 4 increase in permeability. As expected, hydrate accumulates more quickly in the permeable layer.

Because hydrate precipitation modifies the pore space available for continued growth, the higher S_h within the layer raises methane solubility with respect to the adjacent fine-grained sediments promoting a diffusive flux of methane out of the layer (Fig. II.1c; Case 2). This has the effect of smoothing out the S_h profile at the edges of the stratigraphic boundary. In Figs. II.2a-b, the influence of pore architecture produces notable differences in the S_h profile compared to a model neglecting these effects (dashed black line). The combined effects of intrinsic pore size and enhanced permeability (Fig. II.2c) produce a zone of high hydrate saturation within the permeable layer that is flanked by broader, but lower magnitude (with respect to S_h within the layer) hydrate spikes. Enhanced fluid flow also increases the rate at which the HFR diminishes in width.

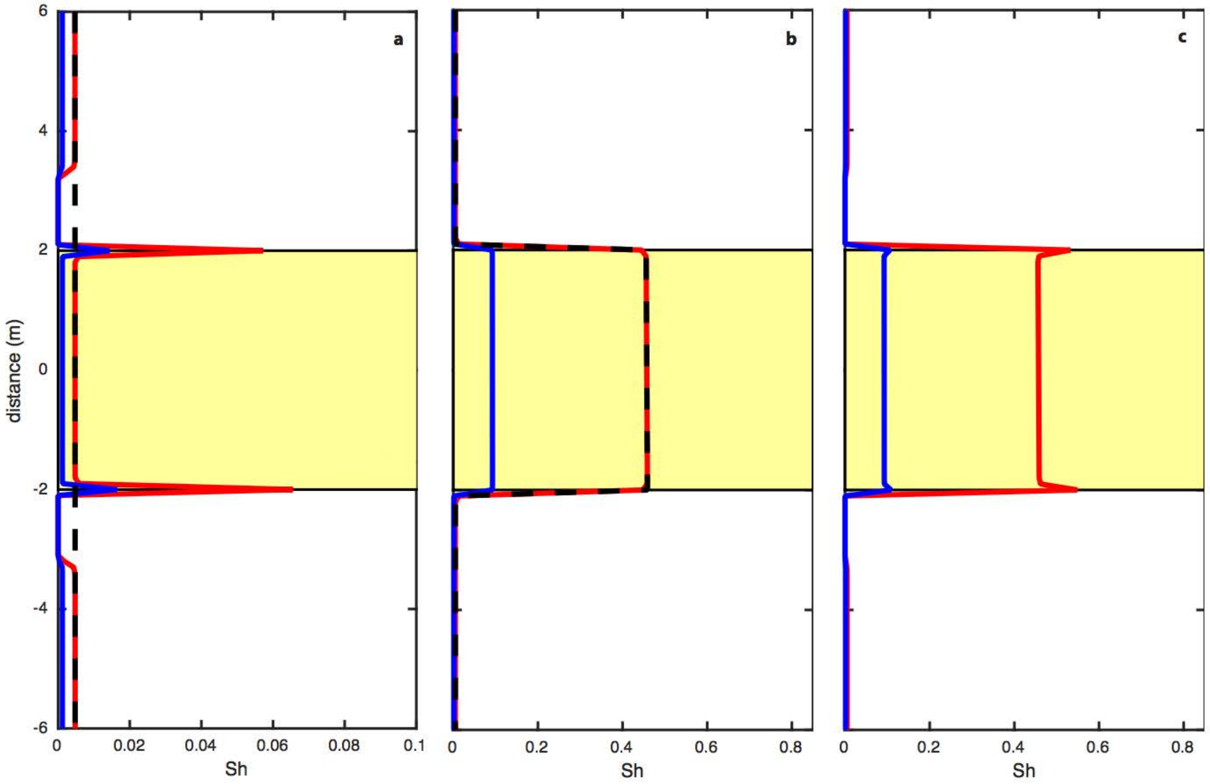

Figure II.3. Hydrate saturation profiles for fine- and coarse-grained undercooling values of 0.01 °C and 0.001 °C (representing a factor of 2 change in pore size). Solutions are drawn at model output times of 2 kya (blue line) and 8 kya (red line). The white and yellow backgrounds identify fine- and coarse-grained regions, respectively. The dashed black lines show hydrate saturation at 8 kya without accounting for pore size effects on methane solubility. (a) Hydrate saturation profiles neglecting enhanced advective flux through the more permeable layer. (b) Hydrate saturation profiles neglecting the influence of intrinsic pore size on methane solubility. (c) The predicted hydrate saturations accounting for both pore size and permeability variations.

We now consider the formation of hydrate in the presence of a stronger contrast in undercooling (Fig II.3). The background undercooling is kept at 0.01 °C and the layer undercooling is defined as 0.001 °C. This difference corresponds to a layer that is more permeable by a factor of 100. Given the substantial increase in the flow velocity, and hence rate of methane accumulation, we decrease our model runtime by a factor of 4/100 (i.e. the ratio of the permeability contrasts in each model; 8 kya). In Fig. II.3a we again show only the effect of pore size on hydrate growth. Because the hydrate spikes are diffusive features, the reduced modeling time results in a significantly smaller saturation anomaly (note the smaller S_h scale in

Fig. II.3a.). Enhanced advection within the layer causes high rates of hydrate growth (Fig. II.3b). The change in S_h at the layer boundaries remains sharp, as too little time has passed for diffusive transport to smooth the S_h profile. The combined effect is a S_h profile that is dominated by flow focusing (Fig. II.3c). These two examples (Figs. II.2 and II.3) demonstrate that pore size and permeability have distinct and pronounced influence on the geometry of hydrate deposits.

II.3.2 Evolution of hydrate spikes

The evolution of the HFR and hydrate spike is sensitive to the contrast in undercooling and the rate of advective methane supply (*Rempel*, 2011). Thus, the distribution of hydrate can be used to infer sediment properties and pore fluid velocities. For example, the examples shown in Fig. II.2. and II.3. reveal obvious differences in the hydrate distribution that results when just the grain size within the anomalous layer is changed and all other variables are kept constant. Further calculations, summarized in Fig. II.4. demonstrate the effects on hydrate spike amplitude that accompany changes in dip angle. Further calculations extend the results presented by *Rempel* (2011) for the $\theta = 0$ case and demonstrate how the spike width and HFR extent also vary with the controlling parameters, including whether the orientation places the coarse-grained material above or below the more fine-grained medium.

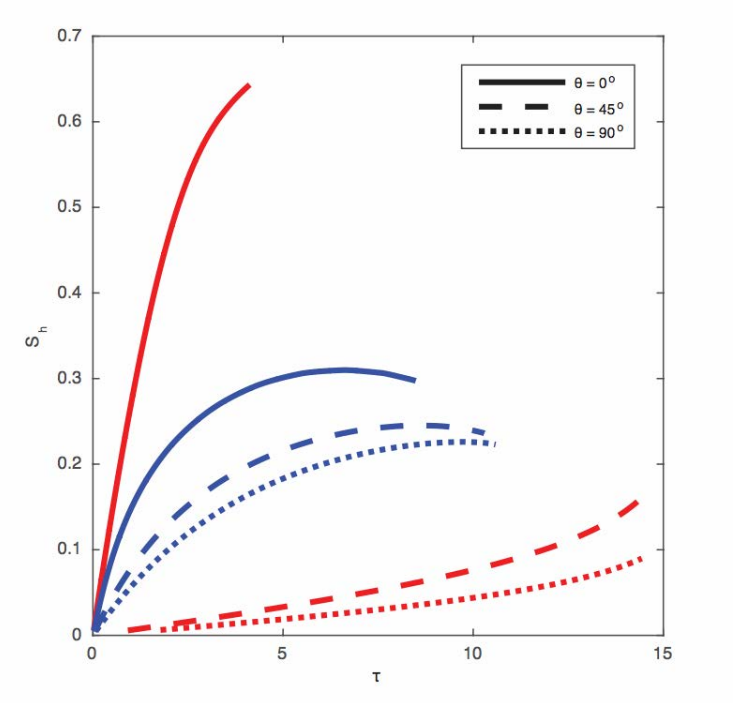

Figure II.4. Dependence of hydrate spike amplitude on undercooling contrast and layer dip. The hydrate saturation at the boundary between fine- and coarse-grained sediments is plotted as a function of non-dimensionalized time (product of the model run time and vertical fluid velocity within the permeable layer divided by the width of the GHSZ) for a layer boundary at 300 m depth. The amplitude of the spike is defined with respect to the hydrate saturation within the permeable layer. Red curves show the case for $\Delta T_{fcourse}/\Delta T_{ffine} = 10$ and blue shows $\Delta T_{fcourse}/\Delta T_{ffine} = 2$. The solid, dashed, and dotted lines trace hydrate spike evolution for a layer dipping 0°, 45°, and 90° from horizontal, respectively. The layer dip modulates the degree of flow focusing. At larger undercooling contrasts, where the predicted advective fluxes are greatest within the layer, the time available for spike growth is limited. The decrease in amplitude of the blue curves at greater times is a result of spike migration.

II.4. Discussion and Conclusions

The main conclusions of this modeling exercise are that: (1) Flow focusing effectively limits the amplitude of hydrate spikes by reducing available time for growth. (2) Therefore, low flux environments should be characterized by diffusive hydrate saturation anomalies. (3) Based on the segregation of hydrate and sediment properties, flow velocities and growth times may be estimated.

Qualitatively, our results compare well with those of several known hydrate accumulations. Good examples derive from: (1) the Gulf of Mexico (*Boswell et al.*, 2012) where hydrates seem to be concentrated in meter-scale sand-rich layers without obvious hydrate spike features. This argues for flow focusing controlled hydrate formation. Given the low dip angles of these layers (< 5°) the permeability contrasts must be quite large for hydrate formation rates to be high enough that significant spikes are not pervasive. (2) Northern Cascadia (*Torres et al.*, 2008 and ref. therein), where both flat-lying and dipping strata show evidence for hydrate spike-like saturation anomalies; this may be a good example of more diffusively controlled growth.

Some of the modeling assumptions that we have adopted deserve further scrutiny, with two deserving special mention. (1) For simplicity we invoked values for the initial methane concentration as poised at bulk equilibrium. In reality, flow focusing means methane will accumulate more rapidly in permeable layers. Depending on the degree of flow focusing and elapsed time, hydrate spikes may not have the opportunity to form because the methane concentration in the fine-grained layers stays low and methane is diffusively transported out of the coarser sediment intervals. This may explain the absence of hydrate spikes in some environments (though measurement resolution may also cause them to sometimes elude detection). (2) The latent heat of hydrate formation and advective effects were both neglected in defining the temperature profile. At high enough rates of hydrate formation, the latent heat of formation can become significant enough to shift three-phase equilibrium (*Smith et al.*, 2014) potentially resulting in stable free gas. However, given the relatively thin width of the permeable layers considered here, layer-normal diffusion of such thermal perturbations is expected to be rapid. A fully 2D model (and more accurate thermodynamic model) would be required to explore this further. It would be interesting to see what fluid velocities would be required to maintain high enough temperature for free gas. In this way, methane vents found in association with faults (e.g. *Gay et al.*, 2007) may not require free gas transport from below BGSZ.

Section III. examines some of the implications of the hydrate distributions discussed in this work, specifically, the potential for concentrated hydrate anomalies to dissociate and alter submarine slope stability.

III. Hydrate dissociation and slope stability

This section concerns the potential for hydrate dissociation to perturb the stability of shallow submarine slopes and produce landslides. This portion of our study constituted a portion of the PhD research and subsequent Postdoctoral work conducted at the University of Oregon by Alexander Handwerger, with assistance from Robert Skarbek; a modified version will soon be submitted for publication in a peer-reviewed journal as "Submarine landslides triggered by rapid dissociation of high-saturation hydrate anomalies", by Alexander L. Handwerger, Robert M. Skarbek, and Alan W. Rempel

III.1. Abstract

Submarine landslides occur along continental margins at depths that often intersect the gas hydrate stability zone, prompting suggestions that slope stability may be affected by perturbations that arise from changes in hydrate stability. Here, we develop a numerical model to identify the conditions under which the dissociation of gas hydrates results in slope failure. Specifically, we focus on high-concentration hydrate anomalies at fine- to coarse-grained stratigraphic boundaries that are prone to large changes in effective stress, sediment permeability, and cohesion over small (m-scale) distances. We evaluate slope behavior before and after hydrate dissociation using an infinite slope stability analysis and a rate- and state-dependent frictional model. Stable hydrate anomalies can transmit bridging stresses that significantly decrease the effective stress at sediment contacts and prevent normal sediment consolidation. Despite these reductions in effective stress, large hydrate concentrations increase the overall slope stability due to large (*O* MPa) increases in effective cohesion. However, when the hydrate anomalies dissociate there is a loss of cohesion and increase in effective stress that causes the surrounding sediment grains to rapidly consolidate and generate excess pore pressures that can trigger slope failure. Predictions from our rate and state model indicate that the ensuing slope failure can display either transient or dynamic motion. However, dynamic motion only occurs when the sediment displays rate-weakening properties and the size of the slip surface exceeds a critical nucleation length, h^*, that is typically smaller than the length of submarine landslides. Our results illustrate fundamental mechanisms through which the dissociation of gas hydrates can pose a significant geohazard.

II.2. Introduction

Natural gas hydrates, stored in large quantities beneath the permafrost and in sediments on the continental shelf, have the potential to become a vital clean-burning energy source, but also pose a significant geohazard. Evidence recorded in coastal sediments worldwide suggests that past changes in environmental conditions have caused hydrates to dissociate and trigger large submarine landslides (Kayen and Lee, 1991; Paull et al., 1996). Furthermore, hydrate dissociation has been known to cause gas blowouts during petroleum drilling and has been linked to past climate change (Nisbet and Piper, 1998). Thus, characterizing hydrate-sediment interactions is critical in order to mitigate hazards associated with future natural or anthropogenic environmental change.

Gas hydrates dissociate when changes in the temperature or pressure alter the local equilibrium conditions of the host sediment (e.g. Kvenvolden, 1993). During dissociation, hydrates release water and free gas and create voids in the pore space that can generate excess pore pressures from 1) volumetric expansion (Xu and Germanovich, 2006; Nixon and Grozic, 2007), 2) rapid consolidation of the host sediments (Kvenvolden, 1993; Lee et al., 2010; Sultan et al., 2010), and 3) fluid flow driven by changes in the average pore fluid density (e.g., Simmons et al., 2001; Diersch and Kolditz, 2002). This excess pore pressure acts to reduce the effective stress and lower the frictional strength of the sediment, and therefore, may trigger or increase the likelihood of slope failure.

Several studies have argued for a causal link between hydrate dissociation and the occurrence of submarine landslides (Kayen and Lee, 1991; Paull et al., 1996; Sultan et al., 2004). Paull et al. (1996) hypothesized that hydrate dissociation during the Pleistocene sea-level lowstand could explain an observed increase in the frequency of slope failures offshore the Southeastern United States. Similarly, Kayen and Lee (1991) found that hydrate dissociation during the Pleistocene could explain a clustering of submarine landslides on the Beaufort Sea margin. There is also evidence to suggest that hydrates may have played a role in triggering the Storegga landslide, offshore Norway; with a volume of 3000 km^2, this is one of the largest submarine landslides ever documented (Sultan et al., 2004). Although there have been no direct observations of hydrate dissociation triggering landslides in natural settings, laboratory experiments and numerical models provide strong evidence that excess pore pressures developed during hydrate dissociation at the base of the hydrate stability zone are capable of triggering slope failure (Kayen and Lee, 1991; Sultan et al., 2004; Xu and Germanovich, 2006; Nixon and Grozic, 2007; Liu and Flemings, 2009; Zhang et al., 2015).

In this manuscript we expand upon these previous works and demonstrate how the dissociation of hydrates from within the gas hydrate stability zone (GHSZ) can trigger slope failure. Specifically, we focus on the dissociation of high-saturation hydrate anomalies that form along stratigraphic boundaries as a result of large methane solubility and matrix permeability contrasts that promote localized hydrate growth. In extreme cases, such anomalies are characterized by segregated, lens-like deposits and nodules that form by pushing the sediment particles apart in order to grow. These areas are of particular interest because they involve abrupt changes in strength over short (m-scale) distances. We simulate hydrate distribution using the 1D growth model from Rempel (2011; see also **Section II**) and estimate sediment properties using constitutive relationships with data from Hydrate Ridge, offshore Oregon, USA (Torres et al., 2004; Trehu et al. 2004; Tan et al., 2006; Winters et al., 2006). We then develop a numerical model that 1) tracks the evolution of excess pore pressure as solid hydrate anomalies decay and cause the host sediment to rapidly consolidate and 2) quantifies slip evolution using a rate- and state-dependent friction model.

III.3 High-saturation Hydrate Anomalies

High-saturation hydrate anomalies (referred to as “spikes”) grow in coarse-grained material that is adjacent to hydrate-free (referred to as “holes”) fine-grained material (Clennell et al., 1999; Hornbach et al., 2003; Torres et al., 2008; Malinverno, 2010; Rempel, 2011). These spikes and holes result from local changes in solubility that arise from the surface energy of the hydrate-liquid interface (i.e. capillary effects), which acts to increase solubility where the interface is highly curved (e.g., throats of small pores), and from the wetting properties of the hydrate-mineral interface that enable thin aqueous films to separate these surfaces. The net result is the development of large-amplitude, narrow (meter-scale or less) spikes in hydrate saturation level, adjacent to hydrate-free holes.

The presence of hydrate spikes has important consequences for understanding potential geohazards (and also for resource extraction) because they alter the mechanical strength of their host sediment (Waite et al., 2009; Rempel, 2011). Once a hydrate spike interconnects for distances that are greater than the average pore radius, it begins to unload sediment contacts and support a portion of the overburden. The vertical load transmitted by the hydrate to the sediment matrix is well-approximated by (Rempel, 2011)

$$\sigma_h \approx -\Pi\left[-\frac{\beta}{\beta-1}\left(1-S_h\right)^{1-1/\beta}+\frac{\beta-S_{h\text{base}}}{\beta-1}\left(1-S_{h\text{base}}\right)^{1-1/\beta}\right], \quad (1)$$

where β is a constant exponent > 0 that characterizes changes in methane solubility with hydrate saturation level S_h (volume fraction of pore space), $S_{h\text{base}}$ is the hydrate saturation at the base of the spike, and $\Pi \equiv \rho_h L\varphi\Delta T_f/T$ is the thermomolecular coefficient that scales the strength of the hydrate-particle repulsive forces, with hydrate density ρ_h, porosity φ, latent heat of fusion L, and normalized undercooling for the initial entry of hydrate into the pore space $\Delta T_f/T$. Using a range of parameter values that span those that are expected to be commonly encountered, Rempel (2011) found that hydrate spikes can reduce the effective stress by as much as 10^3–10^6 Pa. Hence, such anomalies have the potential to completely unload the overlying sediment and prevent normal consolidation, even several tens of meters below the sea floor.

III.4. Methods

III.4.1. Numerical Hydrate Reservoir

We use the numerical model from Rempel (2011) to generate a one-dimensional hydrate reservoir. The model accounts for the sediment–hydrate interactions described in **Section III.3** to produce a heterogeneous hydrate distribution. We focus our investigation between 0 and 100 mbsf, because this encompasses the typical range of thicknesses inferred for submarine landslides (Chaytor et al., 2009). Hydrate spikes are generated by inserting coarse-grained sediment layers into the more fine-grained sediment background, leading to preferential growth on the coarser sides of the layer contacts, with the highest saturations occurring right on each stratigraphic boundary (Fig. III.1).

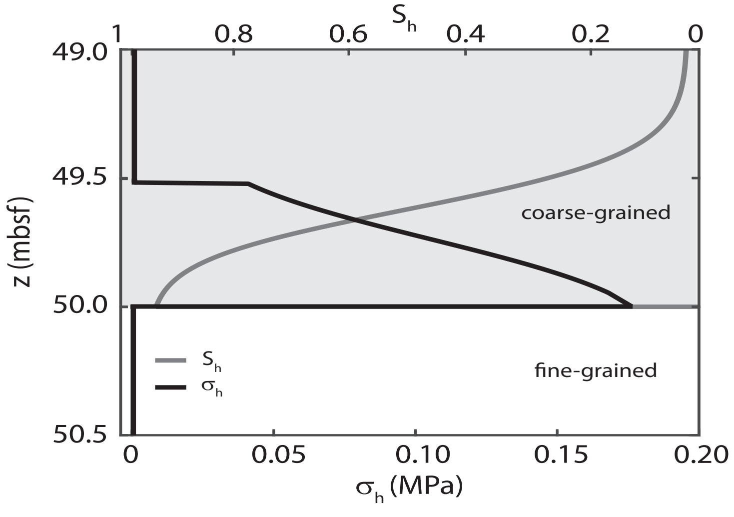

Figure III.1. Idealized representation of load σ_h transmitted by an interconnected hydrate skeleton (black) and corresponding hydrate saturation level S_h near a stratigraphic boundary separating coarse and fine-grained materials. Hydrate grows preferentially in the coarse-grained material, whereas the increased methane solubility in the more fine-grained material (see **Section I**), together with continuity in concentration at the boundary, lead to a hydrate-free region immediately adjacent the high saturation anomaly.

III.4.2. Effective Stress, Porosity, and Pore Pressure in a Hydrate Reservoir

In this one-dimensional treatment, the effective stress σ' in hydrate-bearing sediment increases with depth z according to (Rempel, 2011)

$$\frac{\partial \sigma'}{\partial z} = (1-\phi)(\rho_s - \rho_f)g + (1-\phi)\frac{\eta}{k}u - \frac{\partial \sigma_h}{\partial z} \ , \tag{2}$$

where the first term on the right accounts for buoyancy with sediment density ρ_s, fluid density ρ_f, and gravity g. The second term accounts for the fluid flow (i.e. nonhydrostatic pressure gradient) at vertical Darcy velocity u with permeability k and liquid viscosity η; fluid flow rates in hydrate reservoirs are typically low enough that this contribution is negligible. The third term accounts for the stress gradient transmitted between the hydrate and pore-matrix. To avoid the development of negative effective stresses in the shallow subsurface, we restrict all model simulations to cases with $\sigma' > 0$. Moreover, we note that hydrate can only bare a load so that σ_h is nonzero when the hydrate saturation is sufficiently large (i.e. > 30% for the case depicted in Fig. III.1) that an interconnected hydrate skeleton spans many pores.

For normal consolidation (i.e. hydrate-free or low S_h regions), porosity decreases exponentially with depth according to Athy's law

$$\phi = \phi_0 \exp(-cz) \ , \tag{3}$$

where φ_0 is the porosity at the sea floor, and c is a constant that depends on the lithology and geologic conditions. For hydrate-bearing sediment, porosity increases locally at hydrate spikes such that (Skarbek and Saffer, 2009)

$$\phi = -W\left\{-\exp\left[\frac{-c\sigma'}{g(\rho_s - \rho_f)}\right] + \ln\phi_0 - \phi_0\right\} \ , \tag{4}$$

where W is Lambert's function (Corless et al., 1996).

To quantify the excess pore pressure generated by consolidation during the dissociation of hydrate spikes, we assume dissociation occurs before the excess pore pressure can diffuse away (e.g., Sultan et al., 2004; Nixon and Grozic, 2007; Jiang et al., 2015). The excess pore pressure is defined as $P_{ex} = P - P_{hyd}$, where P is the total pore pressure and P_{hyd} is the hydrostatic pressure. P_{ex} evolves according to

$$\frac{\partial P_{ex}}{\partial t} = \frac{K}{S_s}\frac{\partial^2 P_{ex}}{\partial z^2} \ , \tag{5}$$

where K is the hydraulic conductivity and S_s is the specific storage. The ratio of K and S_s is also known as the hydraulic diffusivity, or consolidation coefficient C_v (see Appendix A in **Section III.8**). All of the above parameters are estimated using data from Hydrate Ridge sediments (Table III.1) (Riedel et al., 2006; Winters et al., 2006; Tan et al., 2006). Using equations (1)-(5), we track the evolution of excess pore pressures as the sediments consolidate.

Symbol	Definition	Value	Reference
	Cohesion		
C	Sediment	$0.03\sigma'$ [Pa]	Ikari and Kopf (2011)
C_h	Hydrate	$2e6S_h$ [Pa]	Waite et al. (2009)
	Density		Daigle and Dugan (2010)
ρ_s	Sediment density	2700 [kg m^{-3}]	
ρ_f	Fluid density	1024 [kg m^{-3}]	
ϕ_0	Surface porosity	0.63 [ ]	Daigle and Dugan (2010)
β	Constant exponent	1.3 [ ]	Rempel (2011)
ζ	Latent heat of fusion	430 [kJ/kg]	Rempel (2011)
$\Delta T_f / T$	Undercooling	0.01 [ ]	Rempel (2011)
c	Athy's constant	7.1e-4 [m^{-1}]	Riedel et al. (2006); Daigle and Dugan (2010)
η	liquid viscosity	8.87e-4 [Pa s]	Daigle and Dugan (2010)
χ	Fluid compressibility	46e-11 [Pa^{-1}]	Daigle and Dugan (2010)
C	Permeability coefficient	11.68	Tan et al. (2004); Daigle and Dugan (2010)
D	Permeability coefficient	-43.9	
a_{rw}	Friction parameter	0.008	Saffer and Marone (2003)
a_{rs}	Friction parameter	0.012	Saffer and Marone (2003)
b	Friction parameter	0.01	Saffer and Marone (2003)
d_c	Characteristic slip distance	4e-4 [m]	
μ_0	Reference friction	0.55	Winters et al. (2006)
v_s	Shear wave speed	910 [m/s]	Yun et al. (2010)
ν	Poisson ratio	0.25	Morris et al. (1991)
L	Length	15000 [m]	
G	Shear modulus	2.2e9 [Pa]	Yun et al. (2010)

Table III.1. Parameters used in model calculations, together with nominal values and sources.

III.4.3 Slope Stability

Slope failure occurs when the gravitational driving stress τ_d equals or exceeds the shear strength τ on the failure surface. The stress balance can be formulated using the infinite slope approximation, which is applicable for slides subjected to uniform conditions (i.e. τ and σ') with lengths and widths that exceed their thickness by orders of magnitude (Chaytor et al., 2009). The slope stability ratio (also known as the Factor of Safety) is defined as

$$\frac{\tau}{\tau_d} = \frac{C' + \sigma'\mu}{\tau_d}\ , \tag{6}$$

where μ is the rate- and state-dependent friction coefficient and C' is the effective cohesion, which increases approximately 30 kPa per MPa of overburden (Ikari and Kopf , 2011) and 20 kPa per percent hydrate saturation (Waite et al., 2009).

In our model we relax the assumption of uniform conditions, while idealizing the landslide as a one-dimensional slip surface embedded in an homogenous elastic medium. Friction on the sliding surface is described using the standard single state-variable law (Dieterich, 1979; Ruina, 1983)

$$\mu = \mu_0 + a\ln\left(\frac{v}{v_0}\right) + b\ln\left(\frac{v_0\theta}{d_c}\right) , \tag{7}$$

where μ_0 is the steady-state friction coefficient at speed v_0, a and b are parameters that dictate whether μ increases or decreases with slip velocity v, and d_c is the characteristic slip distance for the evolution of frictional contacts. The state variable θ evolves according to the Linker-Dieterich law (Linker and Dieterich, 1992])

$$\mu = \mu_0 + a\ln\frac{v}{v_0} + b\ln\left(\frac{v_0\theta}{d_c}\right) , \tag{8}$$

where constant $\lambda \approx \mu_0/3$ (Perfettini, 2000). This state evolution law accounts for additional changes in the friction coefficient that follow effective stress perturbations.

Stress balance along the length L of slip surface dictates that the gravitation driving stress is primarily balanced by frictional resistance, with differential motion resisted by elastic interactions, and inertial effects arising at high slip speeds. An idealized description used for initial calculations has (Segall, 2010)

$$\tau_d + \frac{G}{2\pi(1-\nu)}\int_{-\infty}^{\infty}\frac{\mathrm{d}\delta/\mathrm{d}\xi}{\xi - x}\mathrm{d}\xi = \mu\sigma' + \frac{G}{2v_s}v , \tag{9}$$

where ν is the Poisson ratio, v_s is the shear-wave speed, G is the shear modulus, and the integral dependence on $\mathrm{d}\delta/\mathrm{d}\xi$ accounts for the effects of a heterogeneous slip distribution at local coordinate x. The second term on the right is the "radiation-damping" approximation for inertial effects, which becomes important at dynamic slip speeds $v_{\mathrm{dyn}} \sim 2\sigma' a v_s/G$ (Rice, 1993). The second term on the left is the elastic stress, which is approximated for a dislocation in a whole space. While a more rigorous approach would account for changes in the shear stress and normal stress due to slip near a free surface, the full space model has been found to adequately describe landslide behavior when the length of the initial slip patch is much shorter than the depth below the free surface (Viesca and Rice, 2012). Ongoing efforts to extend this work and incorporate the more complicated treatment of elastic effects that accounts for free surface effects are somewhat more cumbersome, though not overly complicated. However, our focus here on the essential behavior of the system leads us to prefer to omit these effects and retain the idealized description given in equation (9).

Finally, we outline the potential landslide failure modes described by the rate and state friction model. Landslides (and faults) characterized by rate and state friction can exhibit 1) stable sliding, 2) transient sliding, and 3) dynamic (i.e. catastrophic) sliding (Rubin, 2008; Skarbek et al., 2012; Handwerger et al. 2016). Stable or transient sliding can occur for landslides that display rate-strengthening or rate-weakening properties, defined such that $a > b$ or $a < b$, respectively. However, dynamic sliding can only occur for rate-weakening landslides with slip patch dimensions that exceed a critical nucleation length h^* that is given by Dieterich (1979)

$$h^* = \frac{G d_c}{\sigma'(b-a)} , \tag{10}$$

Handwerger et al. (2016) showed recently that h^* for landslides can range from tens of meters to tens of kilometers.

III.5. Results

III.5.1. Effective Stress and Porosity

Figure III.1 shows the estimated effective stress perturbation and saturation profiles for a representative hydrate spike located 50 mbsf. Once the hydrate saturation increases beyond a threshold level (i.e. $S_h > 0.3$), the effective stress decreases progressively as the hydrate begins to support part of the overburden. Further increases in the hydrate saturation enable the hydrate to support a larger fraction of the overburden and further reduce the effective stress. For the example displayed here, the maximum reduction in effective stress is 0.19 MPa (approximately 20% of background effective stress levels), which coincides with the highest hydrate saturation located at the base of the hydrate spike. This reduction in effective stress is accompanied by a 1.3% increase in sediment porosity, when compared to normal consolidation. It is this increase in porosity that sets the stage for consolidation after the hydrate spike dissociates.

III.5.2. Slope Stability

Despite the large reduction in effective stress imparted by the hydrate spike, we find that slope stability actually increases significantly when the stable hydrate is present (Fig. III.2). This increase in sediment strength is due to an increase in the effective cohesion, which acts to overcome the reduced effective stress (Fig III.2). At our representative hydrate spike, slope stability increased by a factor of 9 due to a ~2 MPa increase in effective cohesion. It is also important to note that the modeled slope is inherently stable even when no hydrates are present.

Once the hydrate decays, the additional strength is lost and the sediments consolidate rapidly. This process generates an excess pore pressure that is initially equal to σ_h, but then decays until the pore pressure is hydrostatic. Using our consolidation model, we find the pressure decays rapidly over the first ~40 days, but remains elevated for ~500 days after dissociation.

For the conditions at our representative hydrate spike, the excess pore pressure generated by dissociation is sufficient to trigger immediate slope failure (i.e. $\tau/\tau_d \approx 0.98$). We explore other model outcomes that do not lead to failure in Section III.6. Using our rate and state model, we quantified the spatial and temporal evolution of landslide motion subjected to the excess pore pressure predicted by the consolidation model. We simulate localized hydrate dissociation by applying this stress perturbation to a small region surrounding the uppermost part the landslide (Fig III.3). We performed simulations with both rate-strengthening properties ($a > b$) and rate-weakening properties ($a < b$). In all model runs, the size of the sliding surface and background effective stress are held constant (see Handwerger et al., 2016 for additional model details).

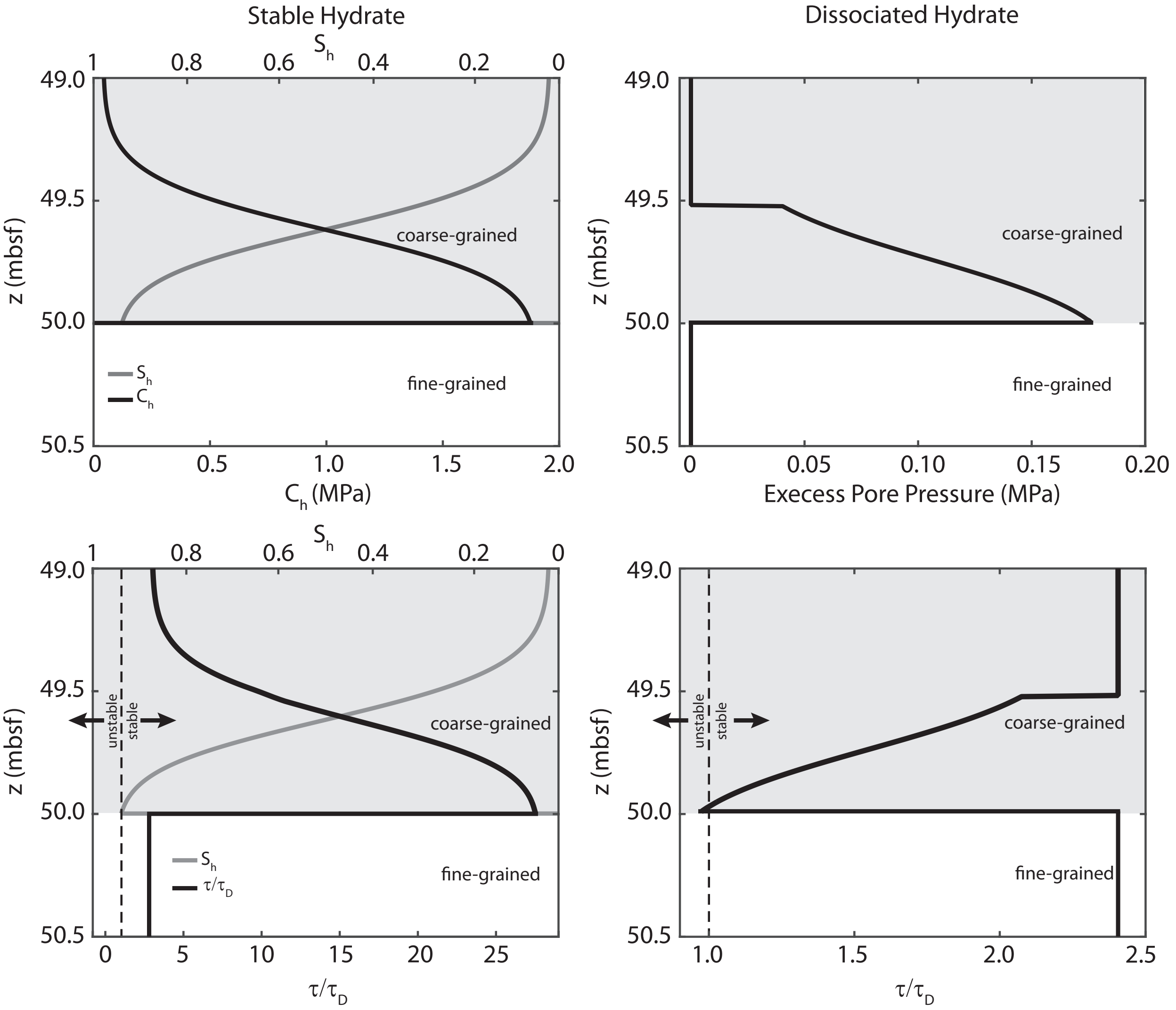

Figure III.2. Upper left: Variation in cohesion (black) and hydrate saturation (grey) within a coarse-grained layer immediately above an adjacent fine-grained layer. Lower left: Shear strength (black) and hydrate saturation (grey) in a stable configuration due to the added cohesion afforded by the hydrate's presence. Upper right: Excess pore pressure generated by compaction following hydrate dissociation. Lower right: Perturbed shear strength, with an excursion near the stratigraphic boundary that reduces strength to below the driving stress, leading to the potential for slope failure.

For simulations with rate-strengthening properties, the modeled landslide displays transient sliding (Fig. III.3). Acceleration begins immediately following hydrate dissociation and propagates down the sliding surface. The highest velocities occur at the location of the stress perturbation and decrease in magnitude as they translate along the sliding surface. Deceleration begins soon after the onset of acceleration, as the frictional strength increases both due to the 'direct effect', which describes the strength change that immediately follows an increase in velocity, and because of the progressive strengthening that occurs as the excess pore pressure diffuses away. After the period of transient slip has passed at a given location, the landslide displays a substantial decrease in velocity due to the stress release during sliding (i.e. the landslide effectively comes to halt).

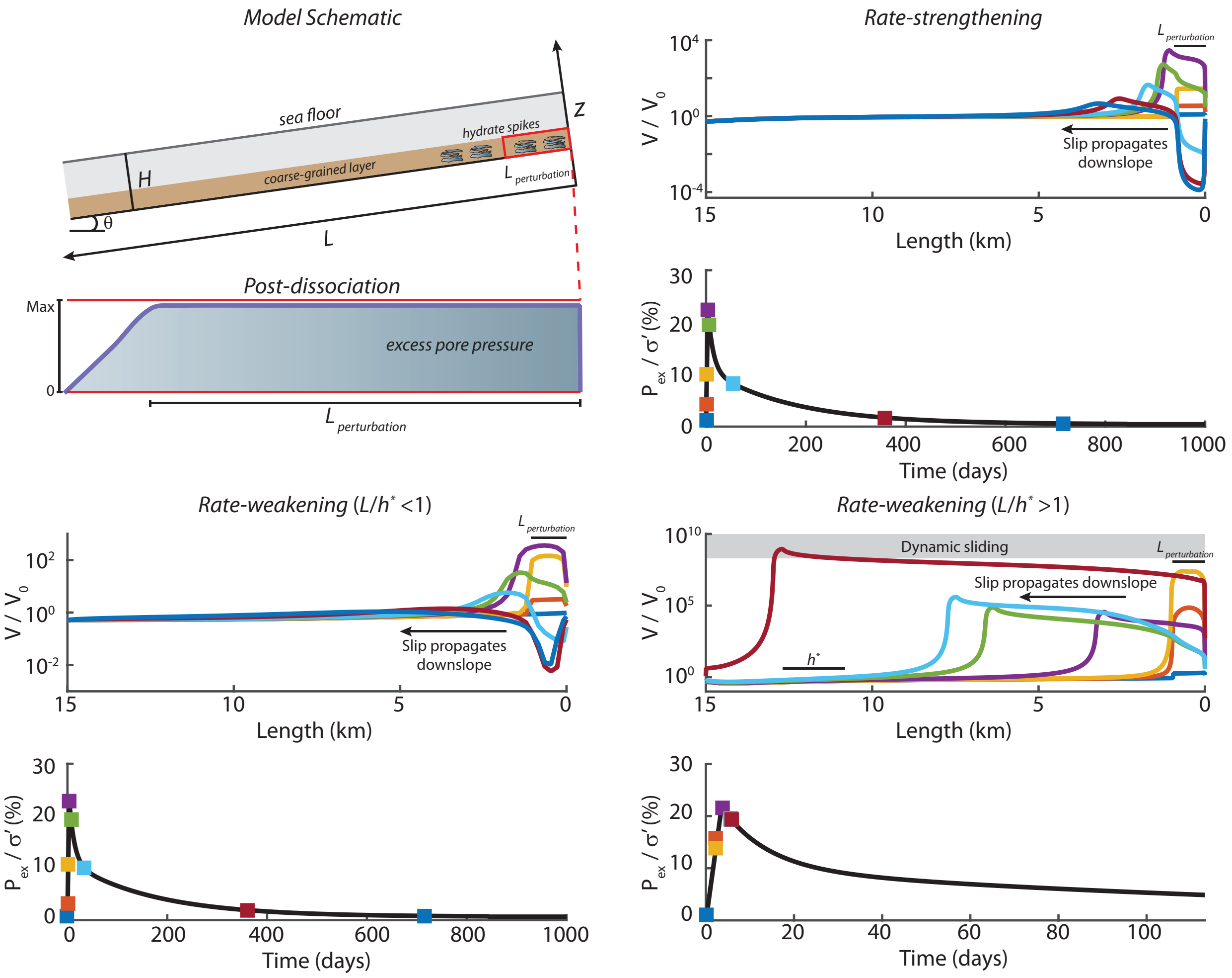

Figure III.3 Potential landsliding behavior due to the hydrate dissociation scenario described in Fig. III.2, for different down-dip perturbation lengths $L_{perturbation}$ and frictional rate dependence. Upper left: Schematic showing model system and perturbation size. Upper right: Rate-strengthening case showing progressive failure that remains in a constant state of force balance (i.e. inertial effects are negligible). Lower left: Rate-weakening case with a perturbation length smaller than required for catastrophic failure, exhibiting similar behavior to that predicted by the rate-strengthening calculations. Lower right: Rate-weakening case with hydrate dissociation leading to a slip perturbation that is large enough to nucleate a dynamic event.

Model simulations with rate-weakening properties displayed both transient and dynamic sliding. When $L/h^* < 1$, the landslide displays transient slip that is similar to the rate-strengthening model. When $L/h^* > 1$, the response is characterized by a runaway instability that transitions to a dynamic sliding regime. In the dynamic regime, the landslide initially is characterized by a period of slow, accelerating slip that spreads along the sliding surface and continues to grow until the resisting stresses can no longer balance the driving stresses, at which point there is a rapid increase in speed and inertial effects become important. Figure III.3 highlights the transition to dynamic sliding by defining a characteristic dynamic slip speed, beyond which the radiation damping term in equation (9) becomes significant.

III.6. Discussion

III.6.1. Dissociation that does not trigger failure

Our model results indicate that the dissociation of high-saturation hydrate anomalies can trigger large submarine landslides. However, there are numerous scenarios where consolidation may not result in immediate slope failure. All else being equal, slope stability is enhanced when the dissociating anomaly is deeper and of lower amplitude. For a given drop in cohesive strength, whether or not immediate failure occurs depends primarily upon the magnitude of the excess pore pressure. Model calculations suggest that a wide range of excess pore pressures can occur given our range in parameter values.

III.6.2. Different Rate and State outcomes

Our rate and state model characterizes multiple failure modes displayed by submarine landslides. In order to predict which failure mode will occur requires information about the effective stress and material properties, all of which are readily available through traditional laboratory tests and geophysical marine exploration. Although rate and state frictional behavior has become a standard empirical constitutive law in fault mechanics and many other fields of the applied sciences (e.g. tribology), measurements of the parameters a, b, and d_c on landslide materials at the relatively low effective stresses (i.e. MPa level or less) of interest are not yet widely available. In choosing these parameters for the model calculations shown above we have relied upon published values from the fault mechanics literature (*Saffer and Marone*, 2009), recognizing that there may be some deviation from these values in the materials that comprise hydrate reservoirs. Nevertheless, the fundamental behavior we have shown is robust in the sense that significant new behavior is not expected to arise even in settings characterized by radically different constitutive parameters.

III.6.3. Elastic stresses during landslides

Our formulation of the stress balance along the failure plane incorporates an elastic interaction term that has been neglected in many previous landslide treatments. As discussed further by *Handwerger et al.* (2016), elastic stress contributions arise naturally in the analogous problem of sliding along tectonic faults, where strain accumulation drives transient slip (i.e. earthquakes) with many of the same characteristics to that observed during landslide motion. Since landslides are driven gravitationally, and the elastic interaction term is negligible both over inter-event timespans and even during events over much of the landslide surface, the neglect of these effects is perhaps understandable. However, it is this elastic interaction term that accounts for changes in longitudinal compression that accompany gradients in slip rate and so determines whether a finite slipping region will grow in size to become unstable, or decay in size and return to static equilibrium. Indeed, this is why elastic parameters enter the definition of h^* given by equation (10) and determine the mode of landslide behavior in response to hydrate dissociation.

III.7. Conclusions

The increase of cohesion and decreased rate of consolidation in high-saturation hydrate anomalies can leave submarine slopes in a state prone for failure upon removal of the hydrate phase. We have developed a framework for quantifying the changes to slope stability and predicting the potential for different modes of slip behavior that can result from the dissociation of hydrate spikes within the two-phase stability zone. Borrowing from the fault mechanics literature, we use a rate-and-state dependent frictional model and incorporate the elastic effects that accompany differential slip rates. This allows us to identify a critical nucleation length h^* that determines the minimum size of a slip patch that will accelerate to catastrophic failure. Smaller slip patches, and those hosted within rate-strengthening materials can still display transient behavior, but with slip rate constrained to always remain slow enough that inertial effects are never important. Our results quantify the potential for gas hydrate dissociation to instigate landslides that both act as a significant geohazard in their own right, and release significant methane volumes into the overlying water column, with possible climactic consequences.

III.8. Appendix A: Parameter interrelations

We define the hydraulic conductivity in terms of permeability such that

$$K = g\rho_f k / \eta \ , \tag{11}$$

and the permeability in terms of porosity as

$$k \ = \ \exp\left(C\varphi \ + \ D\right) \ , \tag{12}$$

where C and D are fit coefficients that depend on the sediment characteristics. Further changes to the permeability occur due to the presence of hydrates such that $k_h \approx k(1-S_h)^2$ (e.g., Liu and Flemings, 2007), however we do not account for such changes since we only consider consolidation following instantaneous dissociation. Lastly, the specific storage, which is the volume of water released from the pore space per unit increase in pressure is defined as

$$S_s \ = \ g\rho_f \ \left(m_v \ + \ \varphi\chi\right) \ , \tag{13}$$

where χ is the fluid compressibility and m_v is the bulk compressibility. Assuming the sediment grains are incompressible, m_v can be defined in terms of porosity as (Skarbek and Saffer, 2009)

$$m_v = \frac{c}{g\left(\rho_s - \rho_f\right)} \ \frac{\phi}{\left(1-\phi\right)^2} \ . \tag{14}$$

IV. Concluding Remarks

In addition to the major accomplishments discussed above, the project team investigated several other avenues of research that have improved our own understanding, but not yet achieved the standard we require to be comfortable with disseminating our results more widely and subjecting them to peer review. In particular, three of our original project milestones were not met and remain subjects of ongoing interest.

1) We have not yet managed to develop the intended quantitative, predictive model to treat segregated hydrate growth using an extension to the formalism developed to describe frost heave (e.g. *Rempel et al.*, 2004). All of the ingredients of this model are in place and we have not encountered any significant difficulties or surprises in our work towards this goal, but our attention was diverted to focus upon other aspects of the project that were deemed more pertinent and we were not able to accomplish this task in the two year timeframe of the grant period.

2) We have not developed a satisfactory chimney nucleation model that describes how these gas-escape features develop in marine sediments. Our original hypothesis pursued the suggestion that the coupled evolution of dissolved gas, heat, salt, and hydrate in submarine sediments in response to a specified advective supply would naturally evolve and give rise to a dynamic three-phase stability boundary that grows towards the seafloor. An initially promising mechanism invoked the effects of solubility variations associated with grain size changes along dipping layers that are known to produce hydrate anomalies and can lead to the formation of salinity anomalies. However, we found that, on their own, such salinity anomalies are unlikely to be sufficiently pronounced to enable the three-phase zones to propagate significant distances. Rather than devote further scarce time and resources to pursue other avenues in this vein, we instead chose to refocus our efforts on the anomaly generation model described in **Section II.**

3) We have not made significant progress on the pockmark spacing hypothesis that we had intended to follow upon the chimney nucleation model described above. We still believe this to be a promising direction for future work. However, because of the encouraging progress we were able to make in the other project areas described in this final report, we deemed it preferable to maintain our focus on completing those project tasks rather than expand the scope of our efforts further during the short timeframe allocated to this project.

The HEROES team is proud of the accomplishments that we have made towards the over-riding project goal of improving quantitative assessments for how climate change alters both reservoir hydrate distribution, and gas transport into the overlying ocean and atmosphere. In addition to the publication on our landslide treatment that is in review (*Handwerger et al.*, 2016) and the three described above that will soon be submitted to leading geoscience journals, we have disseminated project results in multiple presentations at five separate international meetings. Research funded by this grant contributed to the MSc thesis research of one woman scientist, Julia Irizarry, who has embarked upon a promising STEM career. Grant funds also helped to support the PhD research of Alexander Handwerger, who has since been offered a prestigious NASA postdoctoral fellowship to continue his ground-breaking landslide research. Funds for continuing University of Oregon PhD student, Brandon Vanderbeek have helped to broaden the scope of his graduate experience, and will continue to produce dividends as he completes his degree requirements and expands our understanding of geomechanical systems in the Earth's oceanic crust.

Lastly, we acknowledge fruitful interactions with many colleagues over the course of the HEROES project. We particularly appreciate the guidance and support of the three project managers who we reported to during this period, Sandra McSurdy, Joseph Renk, and Adam Tew.

V. REFERENCES

Bischof, J., Scherer, D., Herminghaus, S., Leiderer, P. (1996). Dewetting Modes of Thin Metallic Films: Nucleation of Holes and Spinodal Dewetting. *Phys. Rev. Lett.* 77, 1536–1539. doi:10.1103/PhysRevLett.77.1536

Bahk, J. J., Kim, D. H., Chun, J. H., Son, B. K., Kim, J. H., Ryu, B. J., Torres, M.E., Riedel, M. & Schultheiss, P. (2013). Gas hydrate occurrences and their relation to host sediment properties: results from second Ulleung Basin Gas hydrate drilling expedition, east sea. *Marine and Petroleum Geology*, *47*, 21-29.

Boswell, R. (2009). Is gas hydrate energy within reach? *Science* 325 (5943) 957-958.

Boswell, R., Frye, M., Shelander, D., Shedd, W., McConnell, D. R., & Cook, A. (2012). Architecture of gas-hydrate-bearing sands from Walker Ridge 313, Green canyon 955, and Alaminos canyon 21: northern deepwater Gulf of Mexico. *Marine and Petroleum Geology*, *34*(1), 134-149.

Cahn, J.W., Dash, J.G., Fu, H. (1992). Theory of ice premelting in monosized powders. J. *Cryst. Growth* 123, 101–108. doi:10.1016/0022-0248(92)90014-A

Chatterjee, S., Bhatnagar, G., Dugan, B., Dickens, G. R., Chapman, W. G., & Hirasaki, G. J. (2014). The impact of lithologic heterogeneity and focused fluid flow upon gas hydrate distribution in marine sediments. *Journal of Geophysical Research: Solid Earth*, 119(9), 6705-6732.

Chaytor, J. D., S. Uri, A. R. Solow, & Andrews B.D. (2009). Size distribution of submarine landslides along the US Atlantic margin, *Marine Geology*, 264 (1), 16–27.

Clennell, M. Ben, Hovland, M., Booth, J.S., Henry, P., Winters, W.J. (1999). Formation of natural gas hydrates in marine sediments: 1. Conceptual model of gas hydrate growth conditioned by host sediment properties. *J. Geophys. Res.* 104, 22985. doi:10.1029/1999JB900175

Collett, T.S., Riedel, M., Cochran, J., Boswell, R., Kumar, P., Sathe, A., NGHP Expedition 01 scientific party, (2008). Geologic controls on the occurrence of gas hydrates in the Indian continental margin: Results of the Indian national gas hydrate program expedition 01. *Proceedings of the 6th International Conference on Gas Hydrates* (ICGH 2008).

Cook, A.E., Malinverno, A. (2013). Short migration of methane into a gas hydrate-bearing sand layer at Walker Ridge, Gulf of Mexico. *Geochemistry, Geophys. Geosystems* 14, 283–291. doi:10.1002/ggge.20040

Corless, R. M., G. H. Gonnet, D. E. Hare, D. J. Jeffrey, & Knuth, D.E. (1996), On the lambertw function, *Advances in Computational mathematics*, 5(1), 329–359.

Coxeter, H.S.M. (2002). The Problem of Apollonius. *The American Mathematical Monthly* 109, 5–15.

Daigle, H., Dugan, B. (2011). Capillary controls on methane hydrate distribution and fracturing in advective systems. *Geochemistry, Geophys. Geosystems* 12. doi:10.1029/2010GC003392

Dash, J.G., Rempel, A. W., Wettlaufer, J.S. (2006). The physics of premelted ice and its geophysical consequences. *Rev. Mod. Phys*. 78, 695–741. doi:10.1103/RevModPhys.78.695

Davie, M. K., & Buffett, B. A. (2001). A numerical model for the formation of gas hydrate below the seafloor. *Journal of Geophysical Research: Solid Earth*, *106*(B1), 497-514.

Davie, M., Zatsepina, O., Buffett, B. (2004). Methane solubility in marine hydrate environments. Mar. Geol. 203, 177–184. doi:10.1016/S0025-3227(03)00331-1

Davis, E. E., Hyndman, R. D., & Villinger, H. (1990). Rates of fluid expulsion across the Northern Cascadia Accretionary Prism: Constraints from new heat row and multichannel seismic reflection data. *Journal of Geophysical Research: Solid Earth*, 95(B6), 8869-8889.

Daigle, H., & Dugan, B. (2011). Capillary controls on methane hydrate distribution and fracturing in advective systems. *Geochemistry, Geophysics, Geosystems*, *12*(1).

De Gennes, P.G. (1985). Wetting: Statics and Dynamics. *Rev. Mod. Phys.* doi:10.1103/RevModPhys.57.827

Denoyel, R., Pellenq, R.J.M. (2002). Simple phenomenological models for phase transitions in a confined geometry. 1: Melting and solidification in a cylindrical pore. Langmuir 18, 2710–2716. doi:10.1021/la015607n

Dewangan, P., Sriram, G., Ramprasad, T., Ramana, M.V., Jaiswal, P. (2011). Fault system and thermal regime in the vicinity of site NGHP-01-10, Krishna–Godavari basin, Bay of Bengal. *Mar. Pet. Geol*. 28, 1899–1914. doi:10.1016/j.marpetgeo.2011.03.009

Dickens, G. R., Castillo, M. M., & Walker, J. C. (1997). A blast of gas in the latest Paleocene: Simulating first-order effects of massive dissociation of oceanic methane hydrate. *Geology*, *25*(3), 259-262.

Diersch, H.-J., & O. Kolditz (2002), Variable-density flow and transport in porous media: approaches and challenges, *Advances in Water Resources*, 25 (8), 899–944.

Dieterich, J. H. (1979), Modeling of rock friction: 1. Experimental results and constitutive equations, *Journal of Geophysical Research: Solid Earth*, 84(B5), 2161– 2168.

Duan, Z., Møller, N., & Weare, J. H. (1992). An equation of state for the CH 4-CO 2-H 2 O system: I. Pure systems from 0 to 1000 C and 0 to 8000 bar. *Geochimica et Cosmochimica Acta*, *56*(7), 2605-2617.

Garvin, J.W., Udaykumar, H.S. (2006). Effect of a premelted film on the dynamics of particle-solidification front interactions. *J. Cryst. Growth* 290, 602–614. doi:10.1016/j.jcrysgro.2006.01.018

Gay, A., Lopez, M., Berndt, C., & Seranne, M. (2007). Geological controls on focused fluid flow associated with seafloor seeps in the Lower Congo Basin. *Marine Geology*, *244*(1), 68-92.

Handwerger, A. L., A. W. Rempel, R. M. Skarbek, J. J. Roering, and G. E. Hilley (2016), Rate-weakening friction characterizes both slow sliding and catastrophic failure of landslides, In review for *Proceedings of the National Academy of Science*.

Hansen-Goos, H., Wettlaufer, J.S. (2010). Theory of ice premelting in porous media. *Phys. Rev. E* 81, 1–13. doi:10.1103/PhysRevE.81.031604

Henry, P., Thomas, M., & Clennell, M. B. (1999). Formation of natural gas hydrates in marine sediments, 2, Thermodynamic calculations of stability conditions in porous sediments. *Journal of Geophysical Research*, *104*, 23-005.

Hornbach, M. J., W. S. Holbrook, A. R. Gorman, K. L. Hackwith, D. Lizarralde, & I. Pecher (2003), Direct seismic detection of methane hydrate on the Blake ridge, *Geophysics*, 68(1), 92–100.

Ikari, M. J., and A. J. Kopf (2011), Cohesive strength of clay-rich sediment, *Geophysical Research Letters*, 38(16).

Irizarry, J. T. and A. W. Rempel (2015), How methane solubility changes with hydrate saturation, pore size and salt content in polydispersed media, *Proc. 8th Int. Conf. on Gas Hydrates* (ICGH8-2014).

Israelachvili, J.N. (2011). Intermolecular and Surface Forces, 3rd Ed. Academic Press, ISBN: 978-0-12-391927-4

Jiang, M., C. Sun, G. B. Crosta, and W. Zhang (2015), A study of submarine steep slope failures triggered by thermal dissociation of methane hydrates using a coupled CFD-DEM approach, *Engineering Geology*, 190, 1–16.

Judd, A. G., Hovland, M., Dimitrov, L. I., Garcia Gil, S., & Jukes, V. (2002). The geological methane budget at continental margins and its influence on climate change. *Geofluids*, *2*(2), 109-126.

Kayen, R. E., and H. J. Lee (1991), Pleistocene slope instability of gas hydrate-laden sediment on the Beaufort sea margin, *Marine Georesources & Geotechnology* 10(1-2), 125–141.

Kleinberg, R. L., Flaum, C., Griffin, D. D., Brewer, P. G., Malby, G. E., Peltzer, E. T., & Yesinowski, J. P. (2003). Deep sea NMR: Methane hydrate growth habit in porous media and its relationship to hydraulic permeability, deposit accumulation, and submarine slope stability. *Journal of Geophysical Research: Solid Earth*, *108*(B10).

Kofke, D.A. (1993). Direct evaluation of phase coexistence by molecular simulation via integration along the saturation line. *J. Chem. Phys.* 98, 4149. doi:10.1063/1.465023

Krumbein, W. C., & Monk, G. D. (1943). Permeability as a function of the size parameters of unconsolidated sand. *Transactions of the AIME*, *151*(01), 153-163.

Kvenvolden, K. A. (1993), Gas hydrates—geological perspective and global change, Reviews of *Geophysics*, 31(2), 173–187.

Laplace, P.S. Elementary illustrations of the Celestial mechanics of Laplace: part the first, comprehending the first book. London: Printed for J. Murray, 1821.

Lee, J., J. C. Santamarina, & C. Ruppel (2010), Volume change associated with formation and dissociation of hydrate in sediment, *Geochemistry, Geophysics, Geosystems*, 11 (3).

Linker, M., & J. Dieterich (1992), Effects of variable normal stress on rock friction: Observations and constitutive equations, *Journal of Geophysical Research: Solid Earth* 97(B4), 4923–4940.

Liu, X., & P. Flemings (2009), Dynamic response of oceanic hydrates to sea level drop, *Geophysical Research Letters*, 36(17).

Liu, X., & P. B. Flemings (2007), Dynamic multiphase flow model of hydrate formation in marine sediments, *Journal of Geophysical Research: Solid Earth* 112 (B3).

Liu, X., Flemings, P.B. (2011). Capillary effects on hydrate stability in marine sediments. *J. Geophys. Res. Solid Earth* 116, 1–24. doi:10.1029/2010JB008143

Lomba, E., Alvarez, M., Lee, L.L., Almarza, N.G. (1996). Phase stability of binary non-additive hard-sphere mixtures: A self-consistent integral equation study. *J. Chem. Phys*. 104, 4180. doi:10.1063/1.471229

Malinverno, A. (2010), Marine gas hydrates in thin sand layers that soak up microbial methane, *Earth and Planetary Science Letters*, 292 (3), 399–408.

Malinverno, A., Goldberg, D.S. (2015). Testing short-range migration of microbial methane as a hydrate formation mechanism: Results from Andaman Sea and Kumano Basin drill sites and global implications. *Earth Planet. Sci. Lett.* 422, 105–114. doi:10.1016/j.epsl.2015.04.019

Maslin, M., Owen, M., Day, S., & Long, D. (2004). Linking continental-slope failures and climate change: Testing the clathrate gun hypothesis. *Geology*, *32*(1), 53-56.

Middleton, G. V., & Wilcock, P. R. (1994). *Mechanics in the earth and environmental sciences*. Cambridge University Press.

Millington, R.J., Quirk, J.P. (1961). Permeability of porous solids. *Trans. Faraday Soc*. 57, 1200. doi:10.1039/tf9615701200

Mualem, Y. (1976). A new model for predicting the hydraulic conductivity of unsaturated porous media. *Water Resour. Res*. 12.

Nisbet, E. G., and D. J. Piper (1998), Giant submarine landslides, *Nature*, 392(6674), 329–330.

Nixon, M., and J. L. Grozic (2007), Submarine slope failure due to gas hydrate dissociation: a preliminary quantification, *Canadian Geotechnical Journal*, 44 (3), 314–325.

Or, D., & Hanks, R. J. (1992). Soil water and crop yield spatial variability induced by irrigation nonuniformity. *Soil Science Society of America Journal*, 56, 226-233. doi:10.2136/sssaj1992.03615995005600010035x

Or, D., Tuller, M. (1999). Liquid retention and interfacial area in variably saturated porous media: Upscaling from single-pore to sample-scale model. *Water Resour. Res*. 35, 3591–3605. doi:10.1029/1999WR900262

Paull, C. K., W. J. Buelow, W. Ussler, and W. S. Borowski (1996), Increased continental-margin slumping frequency during sea-level lowstands above gas hydrate–bearing sediments, *Geology*, 24(2), 143–146.

Perfettini, H. (2000), Frottement sur une faille: Influence des fluctuations de la contrainte normale, Ph.D. thesis.

Rehder, G., Kirby, S. H., Durham, W. B., Stern, L. A., Peltzer, E. T., Pinkston, J., & Brewer, P. G. (2004). Dissolution rates of pure methane hydrate and carbon-dioxide hydrate in undersaturated seawater at 1000-m depth. *Geochimica et Cosmochimica Acta*, *68*(2), 285-292.

Rempel, A. W. (2011). A model for the diffusive growth of hydrate saturation anomalies in layered sediments. J. Geophys. Res. 116, B10105. doi:10.1029/2011JB008484

Rempel, A.W. (2012). Hydromechanical Processes in Freezing Soils. *Vadose Zone J.* doi:10.2136/vzj2012.0045

Rempel, A. W., & Buffett, B. A. (1997). Formation and accumulation of gas hydrate in porous media. *Journal of Geophysical Research: Solid Earth*, *102*(B5), 10151-10164.

Rempel, A. W., Wettlaufer, J.S., Worster, M.G. (2001). Interfacial premelting and the thermomolecular force: Thermodynamic buoyancy. *Phys. Rev. Lett.* 87, 088501. doi:10.1103/PhysRevLett.87.088501

Rempel, A. W., J. S. Wettlaufer & M. G. Worster, M.G.(2004). Premelting dynamics in a continuum model of frost heave, *Journal of Fluid Mechanics* 498, 227-244, 2004.

Rempel, A. W., Worster, M.G. (1999). Interaction between a particle and an advancing solidification front. *J. Cryst. Growth* 205, 427–440. doi:10.1016/S0022-0248(99)00290-0

Rice, J. R. (1993), Spatio-temporal complexity of slip on a fault, *Journal of Geophysical Research: Solid Earth*, 98(B6), 9885–9907.

Riedel, M., P. Long, C. Liu, P. Schultheiss, T. Collett, O. Leg, and S. S. Party (2006), 8. Physical properties of near-surface sediments at southern Hydrate Ridge: Results from ODP Leg 204, in *Proc. ODP, Sci. Results*, 204 [Online].

Rubin, A. M. (2008), Episodic slow slip events and rate-and-state friction, *Journal of Geophysical Research: Solid Earth*, 113(B11).

Ruina, A. (1983), Slip instability and state variable friction laws, *Journal of Geophysical Research: Solid Earth*, 88(B12), 10,359–10,370.

Rose, K.K., Johnson, J.E., Torres, M.E., Hong, W.-L., Giosan, L., Solomon, E.A., Kastner, M., Cawthern, T., Long, P.E., Todd Schaef, H. (2014). Anomalous porosity preservation and preferential accumulation of gas hydrate in the Andaman accretionary wedge, NGHP-01 site 17A. *Mar. Pet. Geol.* 58, 99–116. doi:10.1016/j.marpetgeo.2014.04.009

Saarenketo, T. (1998). Electrical properties of water in clay and silty soils. *J. Appl. Geophys.* 40, 73–88. doi:10.1016/S0926-9851(98)00017-2

Segall, P. (2010), Earthquake and volcano deformation, Princeton University Press.

Simmons, C. T., T. R. Fenstemaker, and J. M. Sharp (2001), Variable-density groundwater flow and solute transport in heterogeneous porous media: approaches, resolutions and future challenges, *Journal of Contaminant Hydrology*, 52 (1), 245–275.

Skarbek, R. M. & D. M. Saffer (2009), Pore pressure development beneath the d́ecollement at the Nankai subduction zone: Implications for plate boundary fault strength and sediment dewatering, *Journal of Geophysical Research: Solid Earth*, 114(B7).

Skarbek, R. M., A. W. Rempel, & Schmidt, D. A. (2012), Geologic heterogeneity can produce aseismic slip transients, *Geophysical Research Letters*, 39(21).

Smith, A. J., Mienert, J., Bünz, S., & Greinert, J. (2014). Thermogenic methane injection via bubble transport into the upper Arctic Ocean from the hydrate-charged Vestnesa Ridge, Svalbard. *Geochemistry, Geophysics, Geosystems*, *15*(5), 1945-1959.

Sultan, N., P. Cochonat, J.-P. Foucher, and J. Mienert (2004), Effect of gas hydrates melting on seafloor slope instability, *Marine Geology*, 213(1), 379–401.

Sultan, N., B. Marsset, S. Ker, T. Marsset, M. Voisset, A.-M. Vernant, G. Bayon, E. Cauquil, J. Adamy, J. Colliat, & Drapeau, D. (2010), Hydrate dissolution as a potential mechanism for pockmark formation in the Niger delta, *Journal of Geophysical Research: Solid Earth*, 115(B8).

Tan, B., J. Germaine, & P. Flemings (2006), Data report: Consolidation and strength characteristics of sediments from ODP site 1244, Hydrate Ridge, Cascadia continental margin, in *Proc. Ocean Drill. Program Sci. Results*, vol. 204, pp. 1–148.

Torres, M., K. Wallmann, A. Tr´ehu, G. Bohrmann, W. Borowski, and H. Tomaru (2004), Gas hydrate growth, methane transport, and chloride enrichment at the southern summit of Hydrate Ridge, Cascadia margin off Oregon, *Earth and Planetary Science Letters*, 226(1), 225–241.

Torres, M., A. M. Trehu, N. Cespedes, M. Kastner, U. Wortmann, J.-H. Kim, P. Long, A. Malinverno, J. Pohlman, M. Riedel, & Collett, T. (2008), Methane hydrate formation in turbidite sediments of northern Cascadia, IODP expedition 311, *Earth and Planetary Science Letters*, 271(1), 170–180.

Trehu, A. M., P. E. Long, M. Torres, G. Bohrmann, F. Rack, T. Collett, D. Goldberg, A. Milkov, M. Riedel, P. Schultheiss, N.L. Bangs, S.R. Barr, W.S. Borowski, G.E. Claypool, M.E. Delwiche, G.R. Dickens, E. Gracia, G. Guerin, M. Holland, J.E. Johnson, Y.-J. Lee, C.-S. Liu, X. Su, B. Teichert, H. Tomaru, M. Vanneste, M. Watanabe, & Weinberger J.L. (2004). Three-dimensional distribution of gas hydrate beneath southern Hydrate Ridge: Constraints from ODP Leg 204, *Earth and Planetary Science Letters*, 222(3), 845–862.

Tryon, M. D., Brown, K. M., & Torres, M. E. (2002). Fluid and chemical flux in and out of sediments hosting methane hydrate deposits on Hydrate Ridge, OR, II: Hydrological processes. *Earth and Planetary Science Letters*, *201*(3), 541-557.

Tuller, M., Or, D. (2005). Water films and scaling of soil characteristic curves at low water contents. *Water Resour. Res*. 41. doi:10.1029/2005WR004142

Viesca, R. C., & J. R. Rice (2012), Nucleation of slip-weakening rupture instability in landslides by localized increase of pore pressure, *Journal of Geophysical Research: Solid Earth*, 117(B3).

Waite, W. F., J. C. Santamarina, D. D. Cortes, B. Dugan, D. Espinoza, J. Germaine, J. Jang, J. Jung, T. J. Kneafsey, H. Shin, K. Soga, W.J. Winters, & Yun, T.-S. (2009), Physical properties of hydrate-bearing sediments, *Reviews of Geophysics*, 47(4).

Watanabe, K., Mizoguchi, M. (2002). Amount of unfrozen water in frozen porous media saturated with solution. *Cold Reg. Sci. Technol*. 34, 103–110. doi:10.1016/S0165-232X(01)00063-5

Weinberger, J. L., & Brown, K. M. (2006). Fracture networks and hydrate distribution at Hydrate Ridge, Oregon. *Earth and Planetary Science Letters*, *245*(1), 123-136.

Wilder, J.W., Seshadri, K., Smith, D.H. (2001). Modeling hydrate formation in media with broad pore size distributions. *Langmuir* 17, 6729–6735. doi:10.1021/la010377y

Winters, W. J., W. F. Waite, D. H. Mason, and L. Y. Gilbert (2006), 26. Physical properties of repressurized sediment from Hydrate Ridge. in Tréhu, A.M., Bohrmann, G., Torres, M.E., and Colwell, F.S. (Eds.) *Proceedings of the Ocean Drilling Program, Scientific Results* Volume 204

Wilen, L.A., Wettlaufer, J.S., Elbaum, M., Schick, M. (1995). Dispersion-force effects in interfacial premelting of ice. *Phys. Rev. B* 52, 12426. doi:10.1103/PhysRevB.52.12426

Xu, W., and L. N. Germanovich (2006), Excess pore pressure resulting from methane hydrate dissociation in marine sediments: A theoretical approach, *Journal of Geophysical Research: Solid Earth*, 111(B1).

Zatsepina, O. Y., & Buffett, B. A. (1997). Phase equilibrium of gas hydrate: implications for the formation of hydrate in the deep sea floor. *Geophysical Research Letters*, *24*(13), 1567-1570.

Zatsepina, O. Y., & Buffett, B. A. (1998). Thermodynamic conditions for the stability of gas hydrate in the seafloor. *Journal of Geophysical Research: Solid Earth*, *103*(B10), 24127-24139.

Zatsepina, O. Y., & Buffett, B. A. (2003). Nucleation of gas hydrate in marine environments. *Geophysical research letters*, *30*(9).

Zhang, X., X. Lu, Y. Shi, Z. Xia, and W. Liu (2015), Centrifuge experimental study on instability of seabed stratum caused by gas hydrate dissociation, Ocean Engineering, 105, 1–9.